Doctoral Thesis

Study on Hydrogen Absorption into High-Strength Low-Alloy Steel During Corrosion in Simulated Atmospheric Environments

(模擬大気腐食環境下における高強度低合金鋼の水素侵入挙動に関する研究)

Xiaole Han

(韓 小樂)

Division of Materials Science and Engineering

Graduate School of Engineering

Hokkaido University

Sapporo, Japan

September 2024

Abstract

Stress corrosion cracking (SCC) is a crucial safety concern of steel structures. The coupled effects of tensile stress and corrosive environments on steel can cause crack growth and lead to unexpected and sudden failure. Currently, a potential issue of SCC is to address the hydrogen-induced problems due to a positive correlation between the strength of a metal and its susceptibility to hydrogen embrittlement. For this reason, the wide utilisation of high-strength low-alloy steels in the construction industry, especially in storage and distribution systems for hydrogen, makes the hydrogen-assistant failure of these components a critical concern. Atmospheric corrosion is an environmental degradation phenomenon of steel structures and is commonly accompanied by hydrogen evolution as a side reaction. A considerable amount of hydrogen is supposed to be produced and subsequently absorbed by the steel, presenting challenges to the material durability of steel infrastructures. It is, therefore, necessary to consider the potential problems of corrosion and understand the mechanisms of hydrogen-assistant cracking of steel during corrosion in atmospheric environments.

The present thesis concentrates on the impact of environmental factors such as relative humidity (RH), temperature, and salt aerosols on corrosion performance and the corresponding hydrogen uptake during atmospheric corrosion of high-strength low-alloy steels. Chapter 1 provides a fundamental overview of the state of knowledge with respect to atmospheric corrosion of steel and hydrogen-assistant cracking, which provides the information required to understand the background and importance of hydrogen-related issues in the scope of atmospheric corrosion.

The main focus of Chapter 2 lies in determining the hydrogen absorption behaviour of steel during corrosion under different RH conditions. RH is a factor of crucial importance since it is responsible for the presence of electrolytes during atmospheric corrosion. When RH reaches a specific value known as deliquescence relative humidity (DRH), the deposited salts on the steel surfaces will absorb moisture from the air to form aqueous electrolyte layers for corrosion to occur. Thus, the effect of RH on the corrosion and hydrogen absorption of steel under NaCl deposit was investigated by controlling the RH at different levels below the DRH

of NaCl during wet-dry cycles. The results suggest that hydrogen absorption into steel can occur even if the surrounding RH is below the DRH of NaCl. The amount of permeated hydrogen increases with higher RH in the dry stage of the wet-dry cycles, which is attributed to the prolonged period of the presence of liquid phase inside the corrosion products.

Chapter 3 assesses the applicability of the Hard and Soft Acids and Bases (HSAB) concept in explaining the effect of metal cations of dissolved salts on corrosion kinetics under salt droplets. An analysis of corrosion and hydrogen permeation of steel under aqueous NaCl, $MgCl_2$, $ZnCl_2$, and $AlCl_3$ solution droplets was conducted to investigate the role of different hygroscopic slats and their metal cations in the cyclic wet-dry corrosion. When corrosion occurs under salt droplets containing Mg^{2+}, Zn^{2+}, and Al^{3+}, cation-containing layers are supposed to form on the steel surfaces and present corrosion resistance. Based on the HSAB concept, the metal cations with higher cation hardness are easier to combine with the hard bases such as H_2O and OH^- of the passive films, forming stable protective passive films against corrosion attack under salt droplets.

Chapter 4 verifies whether the concept of the time of wetness (TOW) is practicable to understand the association between hygroscopic salts and the hydrogen absorption behaviour of steel during wet-dry cycles. After water evaporates and steel surfaces become apparently dry, the hygroscopic property of the salts deposited within the porous rust layers plays a dominant role in the corrosion and hydrogen absorption processes. The salts with low deliquescence values retain the presence of thin electrolyte layers with high chloride concentrations within the porous rust structures, affording a prolonged TOW for corrosion and hydrogen absorption into steel.

Chapter 5 summarises the findings and gives the overall conclusion of the research work. Based on the experimental results and analysis, the TOW and HSAB concepts are applicable in explaining the role of salts in the corrosion and hydrogen absorption activity of high-strength low-alloy steel during atmospheric corrosion. This study suggests that localised pitting and acidification under rust layers are responsible for accelerated hydrogen entry into steel during wet-dry cycles.

Acknowledgements

I am deeply indebted to my supervisor, Assoc. Prof. Masatoshi Sakairi, for his guidance and support throughout five years of academic education. Sakairi-sensei provided me with ample autonomy in my studies, enabling me to have plenty of opportunities to gain new knowledge from multidisciplinary courses, cultivate an intense interest in research work, and of course enjoy life.

I sincerely acknowledge the members of my thesis committee for their time and valuable assistance, including Prof. Naoki Hiroyoshi of the Division of Sustainable Resources Engineering, Prof. Shigenari Hayashi of the Division of Materials Science and Engineering, and Prof. Mikito Ueda of the Division of Materials Science and Engineering, Hokkaido University.

I thank all the members of the Novel Materials Hybrid Engineering Laboratory, past and present, from whom I have learned so much. Other special thanks go to the staff at the Laboratory of XPS analysis, Mr. Keita Suzuki and Ms. Suzuka Yoshida, for their valuable advice and support in technical operations.

I am grateful to the doctoral fellowship from Hokkaido University and Japan Science and Technology Agency for financial support, keeping me focused on the research work to complete this PhD project.

Finally, I am immensely grateful to my parents for their endless support and interest in my studies. Their uninterrupted weekly phone calls were of inestimable value during my life abroad.

Table of Contents

1 Introduction

1.1 Background

Steel, a well-known structural material, has a wide range of applications in the construction industry. Its outstanding performance in mechanical properties like strength, ductility, and fracture toughness makes steel conspicuous among a larger number of engineering materials. In addition to carbon steels, which account for the largest market share of all steel products, high-strength low-alloy (HSLA) steels have been well-developed to meet the increased demands for high performance and cost-efficiency in the competitive material markets [1]. The improved mechanical properties and low cost make HSLA steels widely employed in modern bridges, oil platforms, wind farms, and industrial facilities.

Although selecting steels with a high strength and fracture toughness is usually considered reliable for structure design, a potential issue is the positive correlation between the strength of a metal and its susceptibility to hydrogen embrittlement [2]. When steels come into contact with a hydrogen-containing environment, hydrogen can easily enter and diffuse into the material. As the enhanced strength is usually attributed to the complex microstructure and composition of steel, the introduction of hydrogen will increase the ductile fracture risk of microplastic deformation, leading to durability loss or cracking failure of steel structures [3]. Thus, the extensive usage of HSLA steels in the construction industry makes the hydrogen-induced problems of these steel components a critical concern.

Atmospheric corrosion is a common environmental degradation of steel structures during service. Figure 1.1 illustrates an example of the interaction between HSLA steel and its service environments. When steel structures are exposed to the atmosphere, especially in the marine

environment, atmospheric aerosols such as sea salts can introduce corrosive electrolytes to the steel surface and result in accelerated corrosion [4]. Hydrogen evolution reaction is a side reaction during atmospheric corrosion. A considerable amount of hydrogen is supposed to be produced and subsequently absorbed by the steel, presenting challenges to the material durability of steel infrastructures. For this reason, in addition to fitting the demand for mechanical properties to ensure the safety of steel structures, it is also necessary to consider the potential problems of corrosion and understand the mechanisms of hydrogen-assistant cracking of steel during corrosion in atmospheric environments.

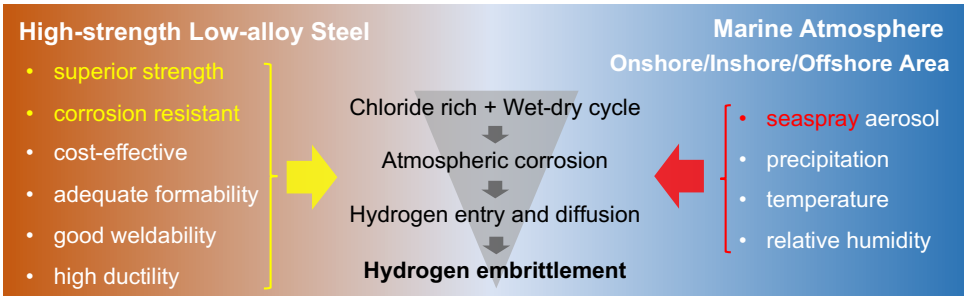

Figure 1.1. Characteristics of high-strength low-alloy steel and marine atmospheric corrosion

1.2 Overview of the State of Knowledge

This section provides a fundamental overview of the state of knowledge with respect to atmospheric corrosion of steel and hydrogen-assistant cracking, which provides the information required to understand the background and importance of hydrogen-induced issues in the scope of atmospheric corrosion.

1.2.1 Atmospheric corrosion of steel

Corrosion is a ubiquitous degradation phenomenon of steel structures that are exposed to

atmospheric environments [5][6][7][8][9]. Natural phenomena like rain, dew, or fog can introduce a water layer to the exposed steel surface during service in the atmosphere. Attributing to the airborne particles, the deposited water layer is usually conductive, providing ionic conduction between the anode and cathode areas on the steel surface for corrosion to occur as an electrochemical process [10]. Since the wide usage of steel products in atmospheric environments, atmospheric corrosion is considered the most predominant feature of the environmental degradation of steel.

All types of corrosion such as uniform corrosion, localized corrosion, and stress corrosion cracking may take place during the corrosion process of steel. However, the initial corrosion step is usually an electrochemical process under droplets on the steel surfaces [11][12][13][14][15]. Figure 1.2 presents a well-accepted model of droplet corrosion. After the formation of an electrolyte droplet on the steel surface from the atmospheric environments, the droplet shape facilitates the access of oxygen to the steel surface through the edge of the droplet and thus establishes an oxygen concentration cell inside the droplet. The edge area where the oxygen concentration is higher acts as the cathode while the central area acts as the anode. As a result, ferrous ions released from the anodic dissolution migrate to the peripheral area and combine with hydroxide ions produced by the oxygen reduction reaction (ORR) to form rust.

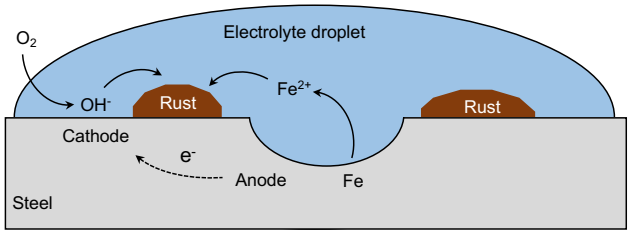

Figure 1.2. Schematic drawing of corrosion process under electrolyte droplet.

As atmospheric corrosion is an electrochemical process, the presence of electrolytes is an essential requirement for corrosion to occur. Multifarious characteristics of the atmosphere, which are responsible for the formation of the electrolyte layer, such as temperature, relative humidity (RH), and aerosol composition, play a critical role in atmospheric corrosion [16][17] [18][19][20]. For instance, when steel structures are employed in the marine environment, sea salt aerosols can introduce hygroscopic particles like NaCl and $MgCl_2$ to the steel surface. Subsequently, as RH increases, the deposited salts absorb moisture from the air and provide an electrolyte for corrosion to take place.

Compared to the rural atmosphere, it has been well known that airborne salts in the marine environment promote a marked increase in the atmospheric corrosion rate [4]. One of the important factors is the abundant concentration of chloride ions in the marine atmospheric environment. The presence of chloride ions can raise the conductivity of the electrolyte and combine with the dissolved ferrous cation produced in the anodic sites of steel structures. The produced chlorides such as $FeCl_2$ accumulate in the rust layers and play a role in accelerating the corrosion process. The $FeCl_2$, for example, can hydrolyses water according to:

$$FeCl_2 + 2H_2O \rightarrow Fe(OH)_2 + 2HCl \quad (1.1)$$

The participation of HCl leads to a significant raising of the acidity in the anodic area and results in further dissolution of steel. The accumulation of Cl^--containing agglomerates, therefore, accelerates the growth of the rust layer [21][22][23].

The corrosion mechanisms of steels under droplets formed in the outdoor environment are different from the bulk electrolyte corrosion due to the daily variations in temperature and RH. When the steel is exposed to the coastal environment, the introduction of the electrolyte to the

steel surface can be enhanced by the deposition of hygroscopic salts such as NaCl and $MgCl_2$. These hygroscopic salts can absorb moisture from the air to form the conductive electrolyte layer as the RH increases and exceeds their deliquescence values. The change in the environmental RH leads to the change in the electrolyte volume on the steel surfaces, which is responsible to the diffusion rate of oxygen to the cathodic area of the steel substrate under the electrolytes.

1.2.2 Hydrogen stress cracking

As a structural material, high-strength steel is not only subjected to corrosion attack in atmospheric environments but also withstands the mechanical loads required for construction components [24][25]. The coupled effects of tensile stress and corrosive environments on steel can cause crack growth and lead to unexpected and sudden failure. This type of material damage is defined as stress corrosion cracking (SCC), and its three essential factors are illustrated in Figure 1.3. Moreover, in the presence of hydrogen environments, hydrogen can easily permeate steel and lower the stress required to initiate and propagate cracks, thus increasing the intensity of SCC. Therefore, the presence of hydrogen during the process of SCC is an important consideration for evaluating the risk of material failure [26][27][28][29][30].

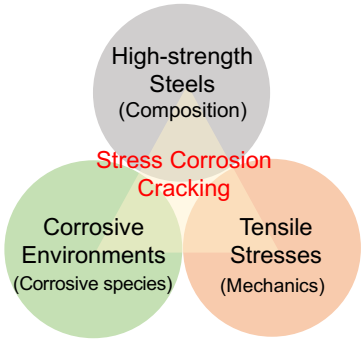

Figure 1.3. Three factors that cause stress corrosion cracking.

Usually, the hydrogen evolution reaction taking place on the steel surface is in the form of hydrogen atom [31]. Since the evolution energy that accompanies the reaction $2H \rightarrow H_2$ is high, the heat evolved from the formation of hydrogen gas needs to be taken away by the steel substrate to get a stable H_2 molecule:

$$H + H + Fe \rightarrow H_2 + Fe \tag{1.2}$$

where Fe represents the steel substrate. Aqueous solutions are considered as potent sources for charging steels with hydrogen due to the presence of abundant hydrogen ions. It is generally accepted that the adsorption and desorption processes of hydrogen in solutions take place according to the Volmer-Heyrovsky-Tafel mechanism [31][32][33]. Figure 1.4 illustrates a typical process of hydrogen uptake into materials.

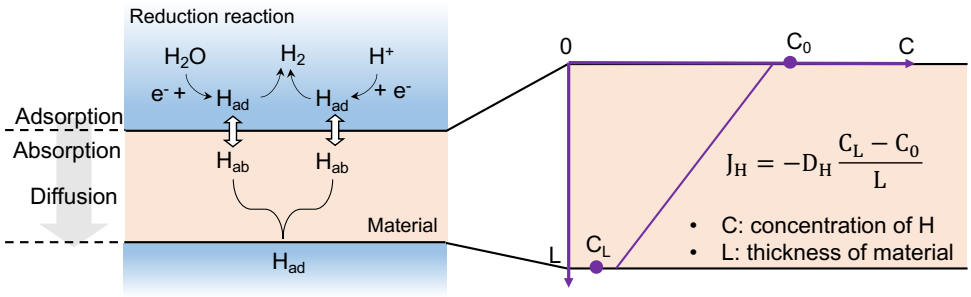

Figure 1.4. Schematic of hydrogen entry, diffusion and detection.

These processes may proceed through the following three steps in acid or alkaline solutions:

Volmer reaction:

$$H^+ + e \rightleftharpoons H_{ad} \tag{1.5}$$

or

$$H_2O + e \rightleftharpoons H_{ad} + OH^- \tag{1.6}$$

Heyrovsky reaction:

$$H_{ad} + H^+ + e \rightleftharpoons H_2 \quad (1.7)$$

or

$$H_{ad} + H_2O + e \rightleftharpoons OH^- + H_2 \quad (1.8)$$

Volmer reaction:

$$2H_{ad} \rightleftharpoons H_2 \quad (1.9)$$

After the surface adsorption of hydrogen, a portion of adsorbed hydrogen can be absorbed into the lattice:

$$H_{ad} \rightleftharpoons H_{ab} \quad (1.10)$$

where H_{ad} and H_{ab} presents the adsorbed hydrogen and absorbed hydrogen, respectively. The absorbed hydrogen atoms can be driven to diffuse through the steel from a region of higher interstitial concentration and towards a region of lower concentration as the formation of a hydrogen concentration gradient in the materials. The diffusion flux density J_H (i.e. the number of hydrogen atoms that diffuses through a unit area in unit time) is proportional to the concentration gradient as described by Fick's first law:

$$J_H = -D_H \left(\frac{C_L - C_0}{L}\right) \quad (1.8)$$

in which D_H stands for the hydrogen permeation coefficient of the material, L is the thickness, and C_0 and C_L stands for the concentration of hydrogen at the entry and exit sides. After a potential is employed at the hydrogen detection side and make it sufficient to ensure rapid ionization of the atomic hydrogen that diffused through the material, the changes in the anodic current of the detection cell represent the instantaneous rate of permeated hydrogen.

1.3 Objectives

The present study focuses on the hydrogen-induced problems of high-strength low-alloy steel during corrosion in atmospheric environments and aims to understand the effects of environmental factors and salt depositions on hydrogen absorption into steel during atmospheric corrosion. More specifically, the objectives are as follows:

(1) To investigate the effect of RH on the corrosion performance of steel under NaCl deposit and to understand the hydrogen absorption behaviour of steel during corrosion with RH variation, especially after the RH decreases below the DRH of NaCl.

(2) To examine the applicability of HSAB concepts in explaining the role of dissolved metal cations in corrosion and hydrogen entry into steel under salt droplets.

(3) To investigate the role of hygroscopic salts in corrosion and hydrogen entry into steel under cyclic wet-dry conditions and to examine the applicability of the TOW concept in explaining the role of salts in corrosion and hydrogen absorption activity under salt deposits.

1.4 Thesis Outline

This thesis is divided into five chapters. The organization is shown schematically in Figure 1.4.

Chapter 1 gives a short introduction to the background and motivation of this research work. A fundamental overview of the state of knowledge for atmospheric corrosion of steel and hydrogen-assistant cracking is provided to understand the subsequent chapters.

Chapter 2 investigates the effect of environmental factor, RH, on the corrosion and hydrogen absorption of steel under NaCl deposit. An atmospheric environment was simulated

by controlling the RH at different levels below the DRH of NaCl during wet-dry cycles.

Chapter 3 focuses on the effect of Na^{+}, Mg^{2+} Zn^{2+}, and Al^{3+} on the corrosion performance under salt droplets. The permeated hydrogen during the corrosion process was measured by electrochemical techniques. The observation of corrosion morphology and analysis of corrosion products were performed in the corrosion tests. The effects of chloride salts on the formation of rust layers and hydrogen entry into steel under salt droplets were discussed based on the hardness of metal cations of salts.

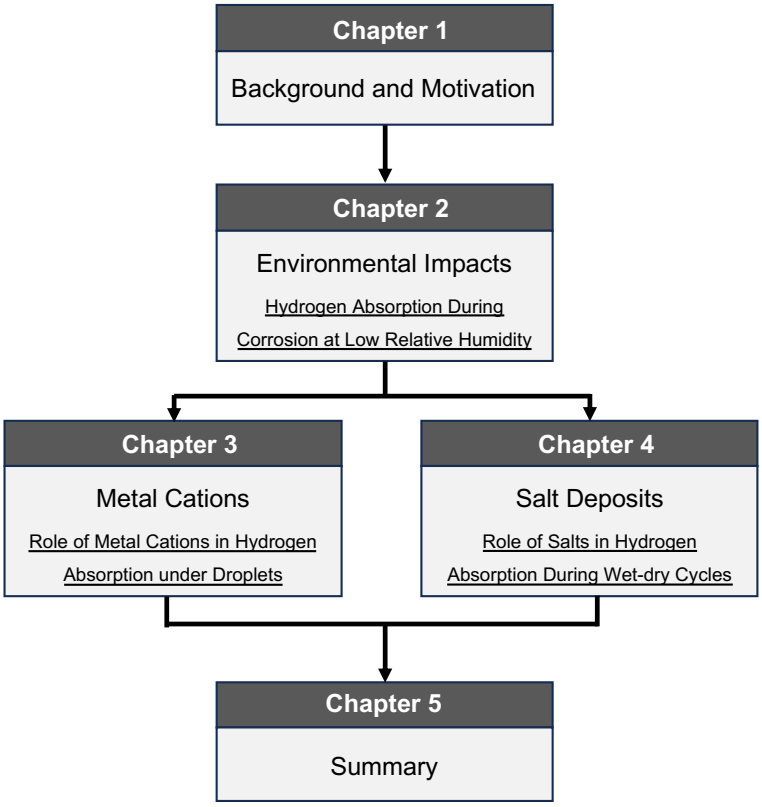

Figure 1.4. Organization of the thesis.

Chapter 4 investigates the corrosion morphology of steel under NaCl, $MgCl_2$, $ZnCl_2$, and $AlCl_3$ deposits and the corresponding hydrogen permeation behaviour using surface characterization techniques and electrochemical methods. The effects of chloride salts on the

hydrogen entry into steel during wet-dry cycles were discussed based on the deliquescence properties of salts.

Chapter 5 summarizes the findings and gives the most significant conclusions from the work.

References

[1] M.F. Ashby, D.R.H. Jones, Engineering materials 1: an introduction to properties, applications and design, Elsevier, 2012.

[2] M. Nagumo, Fundamentals of hydrogen embrittlement, Springer, Singapore, 2016.

[3] S. Eswarappa Prameela, T.M. Pollock, D. Raabe, M.A. Meyers, A. Aitkaliyeva, K.L. Chintersingh, Z.C. Cordero, L. Graham-Brady, Materials for extreme environments. Nat. Rev. Mater. 8 (2023) 81-88.

[4] P.R. Roberge, Atmospheric Corrosion, in: R.W. Revie (Ed.), Uhlig's Corrosion Handbook, third ed., Wiley, New York, 2011, pp. 299-326.

[5] Adikari, A. A. M. T., RGN De S. Munasinghe, and S. Jayathilake, Prediction of atmospheric corrosion–a review, Engineer: Journal of the Institution of Engineers, Sri Lanka 47 (2014).

[6] Y. M. Panchenko, A. I. Marshakov, Long-term prediction of metal corrosion losses in atmosphere using a power-linear function, Corros. Sci., 109 (2016) 217-229.

[7] Alcántara, Jenifer, Daniel de la Fuente, Belén Chico, Joaquín Simancas, Iván Díaz, and Manuel Morcillo, Marine atmospheric corrosion of carbon steel: A review, Materials 10 (2017) 406.

[8] J. Alcántara, D. de la Fuente, B. Chico, J. Simancas, I. Díaz, M. Morcillo, Marine atmospheric corrosion of carbon steel: A review. Materials 10 (2017) 406.

[9] M. Morcillo, I. Díaz, H. Cano, B. Chico, D. de la Fuente, Atmospheric corrosion of weathering steels. Overview for engineers. Part I: Basic concepts, Construction and Building Materials, 213 (2019) 723-737.

[10] P. Pedeferri (Deceased), Electrochemical Mechanism, in: L. Lazzari, L., M.P. Pedeferri

(Ed.), Corrosion Science and Engineering, Engineering Materials, Springer, Cham. 2018, pp. 17-35.

[11] Yu, Jianxing, Huakun Wang, Yang Yu, Zhen Luo, Weidong Liu, and Caimei Wang, Corrosion behavior of X65 pipeline steel: Comparison of wet–Dry cycle and full immersion, Corrosion Science 133 (2018) 276-287.

[12] Zhang, B., J. Wang, B. Wu, X. W. Guo, Y. J. Wang, D. Chen, Y. C. Zhang, K. Du, E. E. Oguzie, and X. L. Ma, Unmasking chloride attack on the passive film of metals, Nature communications 9 (2018) 2559.

[13] Gong, Ke, Ming Wu, Fei Xie, Guangxin Liu, and Dongxu Sun, Effect of dry/wet ratio and pH on the stress corrosion cracking behavior of rusted X100 steel in an alternating dry/wet environment, Construction and Building Materials 260 (2020) 120478.

[14] Katona, R. M., R. G. Kelly, C. R. Bryan, R. F. Schaller, and A. W. Knight, Use of in situ Raman spectroelectrochemical technique to explore atmospheric corrosion in marine-relevant environments, Electrochemistry Communications 118 (2020) 106768.

[15] Gong, Ke, Ming Wu, Fei Xie, Guangxin Liu, and Dongxu Sun, Effect of Cl− and rust layer on stress corrosion cracking behavior of X100 steel base metal and heat-affected zone in marine alternating wet/dry environment, Materials Chemistry and Physics 270 (2021) 124826.

[16] Liu, Shuan, Huyuan Sun, Lijuan Sun, and Huiji Fan. "Effects of pH and Cl− concentration on corrosion behavior of the galvanized steel in simulated rust layer solution, Corrosion Science 65 (2012) 520-527.

[17] Zhang, Xian, Christofer Leygraf, and Inger Odnevall Wallinder, Atmospheric corrosion of Galfan coatings on steel in chloride-rich environments, Corrosion Science 73 (2013) 62-71.

[18] Thee, Ch, Long Hao, Junhua Dong, Xin Mu, Xin Wei, Xiaofang Li, and Wei Ke, Atmospheric corrosion monitoring of a weathering steel under an electrolyte film in cyclic wet–dry condition, Corrosion science 78 (2014) 130-137.

[19] Song, Liying, and Zhuoyuan Chen, The role of UV illumination on the NaCl-induced atmospheric corrosion of Q235 carbon steel, Corrosion science 86 (2014) 318-325.

[20] Dai, Nianwei, Junxi Zhang, Qimeng Chen, Bo Yi, Fahe Cao, and Jianqing Zhang, Effect of the direct current electric field on the initial corrosion of steel in simulated industrial atmospheric environment, Corrosion Science 99 (2015) 295-303.

[21] B.G. Koushik, N. Van den Steen, M.H. Mamme, Y. Van Ingelgem, H. Terryn, Review on modelling of corrosion under droplet electrolyte for predicting atmospheric corrosion rate. J. Mater. Sci. Technol., 62 (2021) 254-267.

[22] T. Nishimura, H. Katayama, K. Noda, T. Kodama, Electrochemical behavior of rust formed on carbon steel in a wet/dry environment containing chloride ions, Corrosion 56 (2000) 935-941.

[23] E. Rocca, H. Faiz, P. Dillmann, D. Neff, F. Mirambet, Electrochemical behavior of thick rust layers on steel artefact: Mechanism of corrosion inhibition, Electrochim. Acta, 316 (2019): 219-227.

[24] Igarashi, Koya, and Masatoshi Sakairi, Effect of surface conditions and specimen composition on hydrogen permeation behavior of coated and uncoated steels during wet and dry corrosion at a constant dew point, Isij International 56 (2016) 465-471.

[25] Ajito, Saya, Eiji Tada, Azusa Ooi, and Atsushi Nishikata, Hydrogen absorption behavior of pre-rusted steels under an NaCl droplet, Journal of The Electrochemical Society 166 (2019) C243.

[26] Zhou, Chengshuang, Xingyang Chen, Zheng Wang, Shuqi Zheng, Xiao Li, and Lin Zhang, Effects of environmental conditions on hydrogen permeation of X52 pipeline steel exposed to high H2S-containing solutions, Corrosion Science 89 (2014) 30-37.

[27] Hao, W., Liu, Z., Wu, W., Li, X., Du, C. and Zhang, D., Electrochemical characterization and stress corrosion cracking of E690 high strength steel in wet-dry cyclic marine environments. Materials Science and Engineering: A, 710 (2018) 318-328.

[28] Moshref-Javadi, Mehrshad, Hossein Edris, Ali Shafyei, Hamidreza Salimi-Jazi, and Ebrahim Abdolvand, Evaluation of hydrogen permeation through standalone thermally sprayed coatings of AISI 316L stainless steel, International Journal of Hydrogen Energy 43 (2018) 4657-4670.

[29] Ajito, Saya, Eiji Tada, Azusa Ooi, and Atsushi Nishikata,Simultaneous measurements of

corrosion potential and hydrogen permeation current in atmospheric corrosion of steel, Isij International 59 (2019) 1659-1666.

[30] Katona, R. M., J. C. Carpenter, A. W. Knight, C. R. Bryan, R. F. Schaller, R. G. Kelly, and E. J. Schindelholz, Importance of the hydrogen evolution reaction in magnesium chloride solutions on stainless steel, Corrosion Science 177 (2020) 108935.

[31] M. Smialowski, Hydrogen in steel: effect of hydrogen on iron and steel during production, fabrication, and use, Elsevier, 2014.

[32] O. Barrera, D. Bombac, Y. Chen, T.D. Daff, E. Galindo-Nava, P. Gong, D. Haley, R. Horton, I. Katzarov, J.R. Kermode, C. Liverani, Understanding and mitigating hydrogen embrittlement of steels: a review of experimental, modelling and design progress from atomistic to continuum, J. Mater. Sci. 53 (2018) 6251-6290.

[33] M. Nagumo, Function of hydrogen in embrittlement of high-strength steels, ISIJ Int. 41 (2001) 590-598.

2 Hydrogen Absorption during Corrosion at Low Relative Humidity

2.1 Introduction

Relative humidity (RH) is one of the crucial environmental factors that are responsible for the presence of electrolytes during atmospheric corrosion. When RH reaches a specific value known as deliquescence relative humidity (DRH), the hygroscopic salt will absorb moisture from the air to form aqueous electrolyte layers [1]. For example, NaCl is the main component of sea salt aerosol and has a DRH of about 75%. When the steel structures are exposed to the marine environments, the deposited NaCl particles will deliquesce and form an electrolyte layer on the steel surface as long as the surrounding RH rises above 75%. As the electrolyte is required for electrochemical reactions, a high RH above the DRH of the deposited salts is usually considered an essential condition for atmospheric corrosion.

Recently, some research work reported the occurrence of considerable corrosion when the RH is less than the DRH of the deposited salts [2] [3] [4]. Schindelholz et al. examined the corrosion response of steel below the DRH of NaCl and found that the corrosion could initiate at 33% RH [5]. They also proposed that the RH of at least 40-50% might be sufficient for a conductive electrolyte to form on NaCl crystals. Haruna et al. studied the hydrogen absorption into Fe under the rust layer containing NaCl and proposed that some NaCl droplets were formed in the rust layer when the RH was lower than the critical RH of NaCl [6]. The published results suggest that the ambient RH above or below the DRH of the deposited salts is not a dependable criterion for determining the occurrence of corrosion during wet-dry cycles. However, the behaviour of hydrogen absorption into steel under controlled RH below the deliquescence values of chloride salts during the corrosion process is still not fully understood.

This chapter investigated the effect of RH on the corrosion and hydrogen absorption of steel under NaCl deposit. Cyclic corrosion test and hydrogen permeation test were conducted under controlled RH and temperature. The RH of the dry condition during wet-dry cycles was controlled at 20%, 55%, 60%, and 65%, which were lower than the DRH of NaCl (75%). The purpose is to understand the hydrogen absorption behaviour of steel during corrosion with RH variation, especially after the RH decreases below the DRH of NaCl.

2.2 Experimental

2.2.1 Sample and salt solution

As high-strength Low-alloy steel was of interest in this study, the material selected was Cr-Mo steel with a Japanese Industrial Standard (JIS) grade of SCM435. This type of steel is currently used for high-pressure storage tanks at hydrogen station in Japan. Its chemical composition is listed in Table 2.1.

Table 2.1. Chemical composition of the steel sample (mass%).

C	Si	Mn	P	S	Cr	Mo	Fe
0.35	0.18	0.74	0.0011	0.0017	1.15	0.15	Bal.

The heat treatment process was conducted as follows: the original steel bar was kept at 850°C for 2 h, oil quenched, and then tempered at 530°C for 3 h. The mechanical property of the steel after heat treatment was tested, exhibiting a yield strength greater than 785 MPa and a tensile strength greater than 930 MPa. The steel bar was machined into samples with

dimensions of 20 mm × 15 mm × 1 mm. The samples were subsequently embedded in cold-curing resin and mechanically ground with SiC grinding papers up to 2400 grit. The polished surfaces (20 mm × 15 mm) were cleaned sequentially with ethanol and highly purified water in an ultrasonic bath for 300 s.

To simulate the corrosion of steel by these chlorides incorporated with airborne droplets, salt solution droplets with volumes of 10 μL were deposited onto the samples and the droplet contact diameters were about 5 mm. NaCl is the most common and abundant airborne salt, and its concentration used in this work was 10 mM to make the amount of deposited chloride close to the actual environments at weathering sites across Japan [7]. The salt solutions were prepared using analytic grade reagents (Kanto Chemical Co., Inc., Japan) and ultrapure water at room temperature.

2.2.2 Hydrogen permeation test

An electrochemical apparatus based on the Devanathan-Stachurski (DS) cell [8] was employed to record the permeation current of hydrogen that was produced on one corroding side and then diffused through the sample. As shown in Figure 2.1, the apparatus consisted of a hydrogen detection cell and an upper exposed area where the corrosion occurred, which were separated by the sample. In order to avoid the instability of current changes due to the passivation of sample surfaces during the anodic polarization in the following hydrogen permeation test, one side of the samples was electroplated with a Ni layer of approximately 1 μm thick using a 0.312 M $NiSO_4$/0.781 M H_3BO_3 solution at a current density of 4 mA cm^{-2} for 720 s. The Ni plating exhibited good reproducibility and was effective for the detection of

permeated hydrogen through the samples.

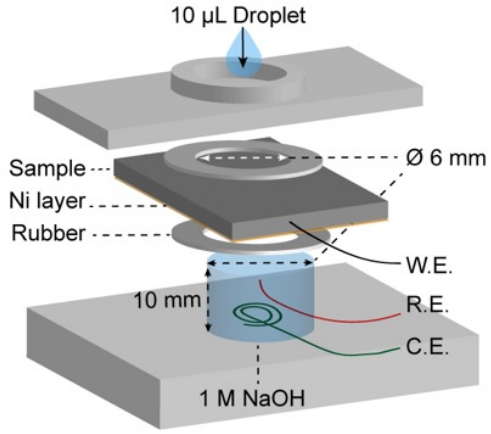

Figure 2.1. Schematic of the electrochemical cell for the measurement of hydrogen permeation currents during corrosion.

The Ni-plated surface of the sample was in contact with the hydrogen detection cell and acted as the working electrode (WE). The counter electrode (CE) and reference electrode (RE) were made of Pt wires of 0.5 mm in diameter and were fixed in the detection cell filled with 1 M NaOH solution. The opposite surface of the sample was prepared for the placement of droplets that would initiate the corrosion. The sample was then bolted between two rubber rings so that both sides had the same exposed area of 28.27 mm^2. The absence of gas bubbles in the detection cell was confirmed before the subsequent polarization procedures.

The hydrogen diffusion coefficient of the sample was also measured using a DS cell as shown in Figure 2.2. The DS cell was designed using was a CAD software (Blender 2.91) and then was fabricated by a 3D printer (Form 2, Forma Labs) using a photo-liquid polymer resin (FLGPCL04) as a raw material. Both sides of the DS cell have a cylinder shape with the same

diameter of 6 mm, the bottom cell has a height of 10 mm and the top one is 15 mm. The bottom cell was the same design as shown in Figure 2.2, which was responsible for hydrogen detection. Another side of the DS cell was used to produce hydrogen as a hydrogen charging cell. Pt wire with a diameter of 0.5 mm was used as an electrode. 0.1 M Na_2SO_4 and a mixed solution (1 mM NaOH + 0.1 M Na_2SO_4) were used as electrolyte in the hydrogen charging cell.

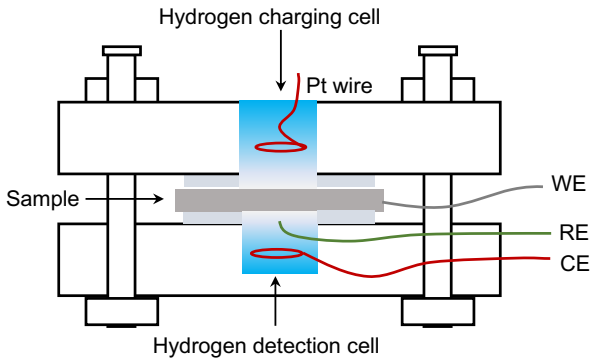

Figure 2.2. Schematic drawing of the DS cell for hydrogen permeation test.

The DS cell was set in an RH and temperature-controlled chamber and its hydrogen detection cell was polarized at -30 mV vs. Pt using a potentiostat (HECS 318C, Fuso, Kawasaki, Japan). After the background current of the detection cell reached lower than 40 nA cm^{-2}, a direct current power supply was used to provide -100 µA and -20 µA constant cathodic currents to the charging cell when 0.1 M Na_2SO_4 was used as electrolyte, whereas a -40 µA constant cathodic current was provided in the case of using a mixed solution (1 mM NaOH + 0.1 M Na_2SO_4). The RH was controlled at 60% to retard the evaporation of electrolyte. The hydrogen permeation tests were carried out in 30°C and 50°C to obtain the hydrogen diffusion coefficients under different temperatures.

2.2.3 Cyclic corrosion test

The assembled electrochemical cell was installed horizontally in a temperature and humidity chamber (IW243, Yamato Scientific Co., Ltd., Japan) as presented in Figure 2.3. Prior to the corrosion test, the sample was pre-polarized at a constant anodic potential of -30 mV vs. Pt until the background current reached a steady value and fell below 20 nA cm^{-2}, which required about 24 h. The anodic potential of -30 mV vs. Pt was sufficient to ensure rapid ionization of the permeated hydrogen atoms from the sample and was employed in all hydrogen permeation tests in the study. 10 mM NaCl aqueous solution with a volume of 10 μL was placed as a droplet on the surface of the sample using a microliter pipette. Simultaneously, the changes in the anodic current attributed to the ionization of diffused hydrogen atoms from the corrosion side were recorded.

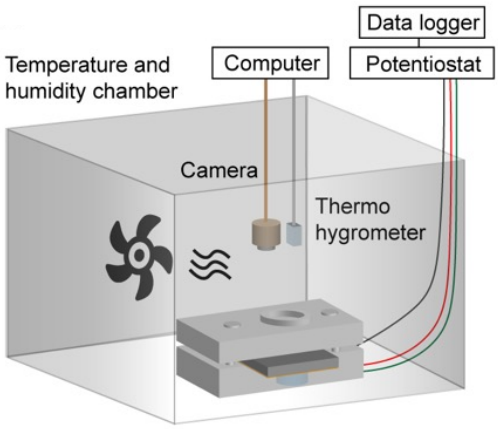

Figure 2.3. Experimental setup for cyclic wet-dry corrosion tests.

A cyclic wet-dry environment was simulated using the temperature and humidity chamber. After the placement of salt solution in the form of droplets on the sample, the temperature and humidity inside the chamber were controlled according to a pre-designed procedure. Wet/dry

cycles were carried out according to four stages (wet period, drying period, dry period, and wetting period) in one cycle as shown in Figure 2.4. The minimum RH value during the wet-dry process was set at 20%, 55%, 60%, and 65%. The RH values at the dry period were lower than the DRH of NaCl. The corrosion process was carried out for 12 cycles (72 h). A thermos-hygrometer was fixed above the sample to ensure that the desired temperature and humidity were achieved throughout the whole experiment. The airflow inside the chamber functioning for air circulation was another essential parameter in the corrosion process, with a velocity of 1.4 m/s above the samples. The cyclic corrosion tests combined with hydrogen detection were carried out at least three times for each salt solution to ascertain the reproducibility of appreciable phenomena during the experiments.

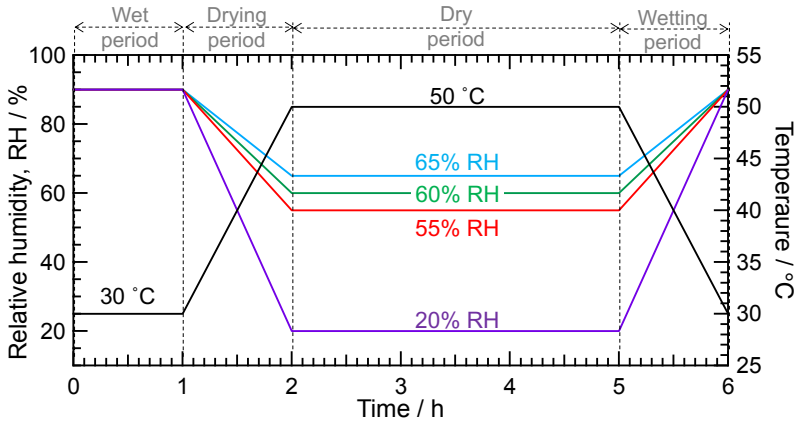

Figure 2.4. Schematic of the changes in RH and temperature during one corrosion cycle.

2.2.4 Surface observation

To understand the corrosion process of steel under cyclic wet/dry conditions, an autofocus USB camera with 1080p resolution was used for surface imaging during the corrosion process of the sample. The surface changes were captured at intervals of 30 s during the cyclic corrosion

test. After the corrosion tests, micrographs of the corroded surface were taken using an optical microscope (OM, MV-550, WRAYMER Inc., Japan).

2.3 Results

2.3.1 Hydrogen permeation coefficient of samples

The sample was initially cathodically charged with hydrogen using 0.1 M Na_2SO_4 at a given constant cathodic current at room temperature. Figure 2.5 (a) shows the transient currents of the sample during cathodic charging. The current begins to increase after hydrogen diffused through the sample and finally reaches a steady value. Diffused hydrogen through the sample under a -100 μA constant cathodic current can be detected early in comparison with the sample under -20 μA. Moreover, the stable value of permeation current under the former condition is much higher than the latter case. This behaviour is attributed to the higher hydrogen diffusion flux under a higher current density.

To inhibit the corrosion phenomenon in the hydrogen permeation tests, a mixed solution with 1 mM NaOH and 0.1 M Na_2SO_4 was used. Results of the time transient of permeation current under this mixed solution are shown in Figure 2.5 (b). The permeation current of sample under 50°C environment begins to increase ahead of that under 30°C, suggesting that temperature plays an important role in the hydrogen diffusion process. As the hydrogen charging process was conducted under a constant hydrogen diffusion flux on the entry side, the hydrogen diffusion coefficient can be determined through the time lag method using the obtained current-time transient data. Hydrogen permeation parameters of samples are listed in Table 2.2. The hydrogen diffusion coefficient of samples under a low temperature shows a

indistinct variation, whereas it increases greatly under a high temperature. This result indicates that temperature presents a significant enhancement on the hydrogen diffusivity.

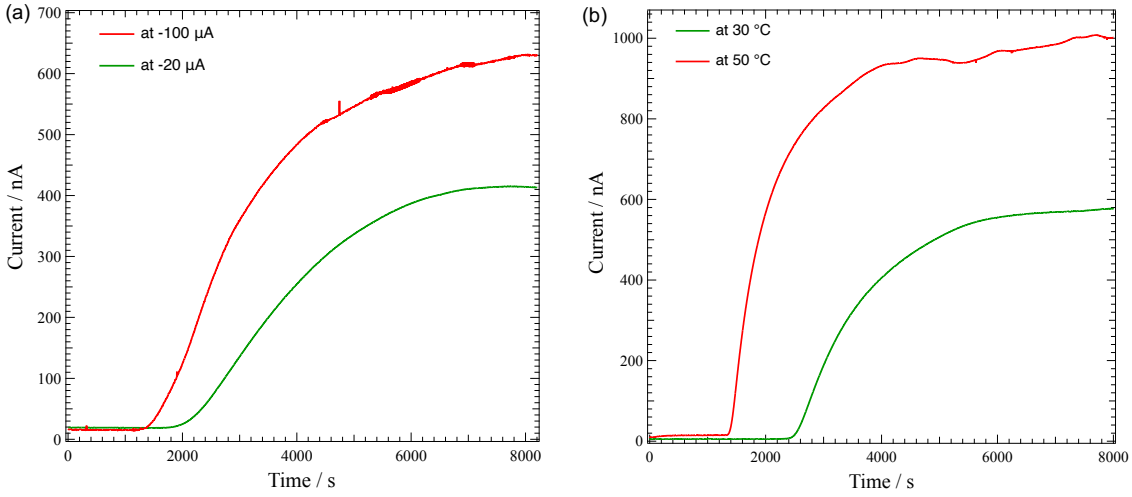

Figure 2.5. Results of transient current of samples after starting galvanostatic cathodic polarization at different currents and temperatures. The electrolyte used in the hydrogen charging cell was (a) 0.1 M Na_2SO_4 and (b) 1 mM NaOH + 0.1 M Na_2SO_4.

Table 2.2. Hydrogen permeation results of samples under different conditions.

Electrolyte	Temperature/°C	Current/μA	i_∞/nA	t_L/s	D/cm^2s^{-1}
0.1 M Na_2SO_4	23	-100	670	3450	1.45×10^{-6}
0.1 M Na_2SO_4	23	-20	414	4050	1.23×10^{-6}
1 mM NaOH + 0.1 M Na_2SO_4	30	-40	398	3800	1.32×10^{-6}
1 mM NaOH + 0.1 M Na_2SO_4	50	-40	594	2050	2.44×10^{-6}

2.3.2 Hydrogen permeation current of samples during cyclic corrosion tests

Figure 2.6 shows the changes in the permeation current of samples under different RH

values in the dry period during cyclic corrosion tests for 12 cycles (72 h). At the initial stage, the currents increase gradually and then tend to keep steady when the temperature is constant at 30 ˚C. The increase in the current is attributed to the increasing temperature from room temperature to 30 ˚C. After the wet period (1 h), the current increases at a rapid rate to reach a peak value with the gradual increase of temperature. When the RH values of the dry period are controlled higher than 60%, the peak values of the current are larger than the other conditions. The drastic increase in the current is attributed to the acceleration of hydrogen evolution reaction and hydrogen diffusion, which can be accelerated by the increasing temperature. The current, except the condition under 55% RH at the dry period, decreases swiftly at the early stage of the dry stage. When the RH at the dry period is controlled higher than 55%, the current keeps at a larger value compared with the wet period. This result indicates that the hydrogen evolution reaction occurs on the steel surface even though the RH is lower than the DRH of NaCl. After the dry period (3 h), the current shows a rapid decrease during the wetting period due to the decreasing temperature.

After the second cycle, the peak value at the beginning of the dry period decreases with the increase of cycle number. Some humps are observed on the shoulder of the currents during the dry stages, which indicates that the hydrogen evolution reaction is accelerated in these periods. In addition, the currents in the dry periods become steady after several cycles. The current under 20% RH becomes steady at the earliest after 2 cycles, while the current under RH higher than 60% takes a long time (about 9 cycles) to drive at a steady value in the dry period. The changes in current of each cycle are comparable after the current keeps at a steady state.

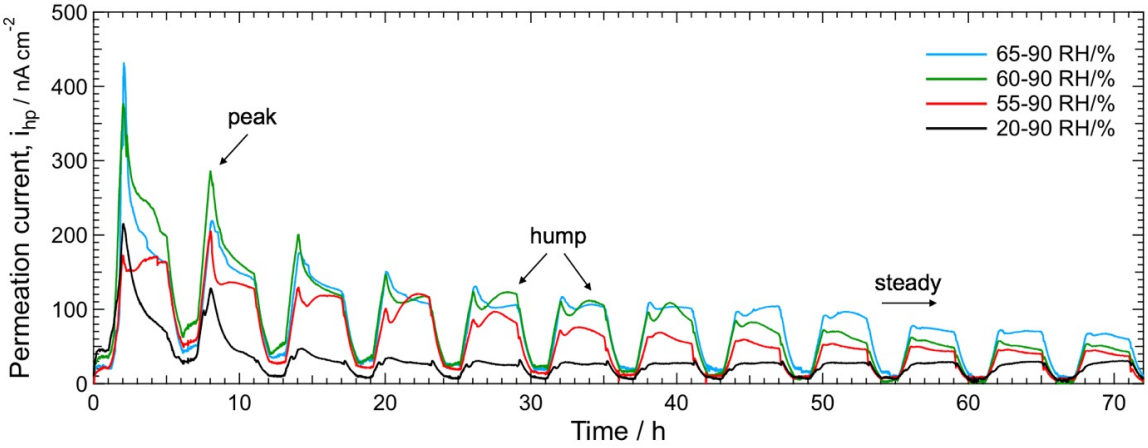

Figure 2.6. Changes in permeation currents during cyclic corrosion tests under different RH values in the dry period.

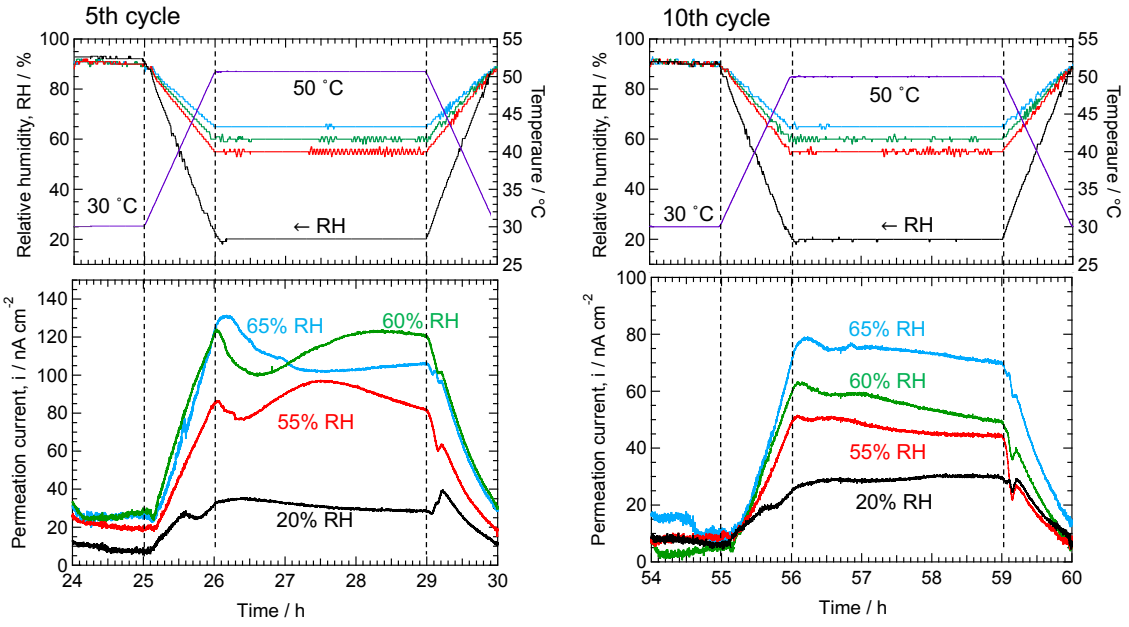

Figure 2.7. Changes in the permeation currents combined with varying temperature and RH during the 5th and 10th cycles.

The expanded images of the changes in the currents during the 5th and 10th cycles of the wet-dry corrosion tests give detailed information as shown in Figure 2.7. The current varies in a lower range at the wet period and then increases at different rates, contrary to the rates at

which RH decreases. In the case of the 5th cycle, although the RH values during the dry period are lower than the DRH of NaCl, the currents under the conditions of 55% and 60% present a significant increase. This phenomenon indicates the occurrence of considerable hydrogen absorption reaction when the RH is lower than the DRH of NaCl. During the 10th cycle, the current values at the dry period of each cycle show a distinct disparity between different RH values and increases with increasing RH. For an entire cycle from wet to dry, the current in the wet period is always lower than the dry period. The current increases and decreases drastically during the drying and wetting periods. These results indicate that temperature and RH play an important role in the hydrogen evolution reaction during wet/dry corrosion processes.

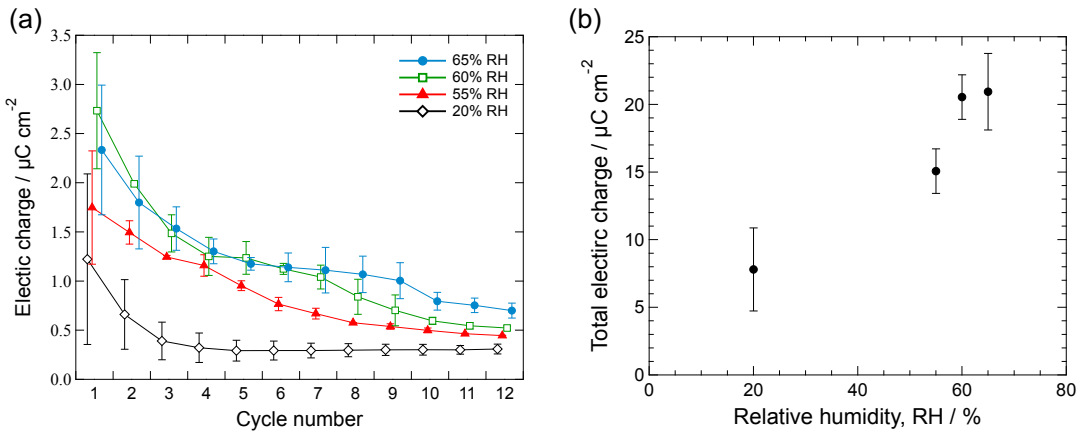

Figure 2.8. (a) The electric charges of each dry period as a function of cycle number. (b) The total electric charge of each wet/dry corrosion test as a function of the RH value during the dry period. The error bars indicate 95% confidence intervals.

The area under the current curve in each cycle represents the electric charge, which is related to the amount of permeated hydrogen. Figure 2.8 (a) shows the electric charge during the dry period of each cycle as a function of cycle number. The electric charge of each cycle

decreases with the increase of the cycle number and tends to keep steady after several cycles. The difference between the electric charges under different RH conditions is not statistically significant during the initial cycles. After the electric charges become steady, there is a significant difference in the charges under controlled RH values. The electric charge of each cycle increases with increasing RH at the dry period. Figure 2.8 (b) reflects the total electric charge during the wet/dry cyclic corrosion test as a function of RH value at the dry period. The hydrogen permeation charge increases with increasing RH. The electric charge is comparable when the RH of dry periods is higher than 60%. These results indicate that the increasing RH at dry periods accelerates the hydrogen evolution reaction.

2.3.3 Surface observation of samples under wet/dry corrosion tests

To understand the relationship between the corrosion process and the hydrogen permeation behaviour, the optical endoscope images of the corrosion process on the specimen surface during cyclic corrosion tests were obtained as shown in Figure 2.9. Initially, 10 mM NaCl solution is placed on the specimen surface and no corrosion products are observed under the droplet (Figure 2.9 (a)). At the wet period of the first cycle (T: 30˚C, RH: 90%), some orange corrosion products are generated on the steel surface under NaCl droplet after 30 min (Figure 2.9 (b)). This means the corrosion reaction with hydrogen evolution initiates under the droplet combined with the changes in the current as shown in Figure 2.6. The orange corrosion products flowed and were scattered in the NaCl solution. At the latter stage of the wet period, the amount of orange corrosion product has spread over the entire droplet area (Figure 2.9 (c)).

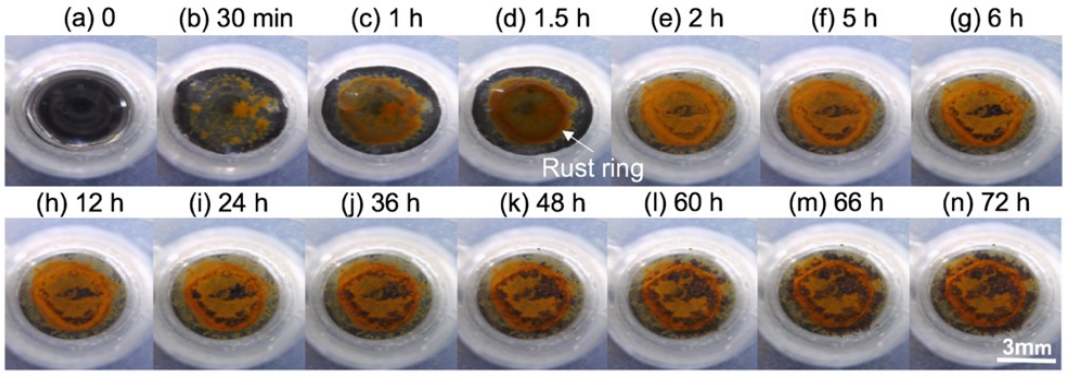

Figure 2.9. Time-sequenced images of the samples during wet/dry cyclic corrosion tests with 55% RH in the dry period.

After the wet period (1 h), the increase in temperature and the decrease in RH accelerate the evaporation of water and promote the formation of corrosion products. This is considered to enhance the hydrogen evolution and result in the rapid increase of the current during the drying period. With the formation of more corrosion defects, more orange rust accumulates on the specimen surface along the perimeter of the droplet to form a perceptible rust ring (Figure 2.9 (d)). The corrosion products spread out adjacent to the rust. These results indicate the corrosion reaction is conducted during the drying period. A thin film of corrosion products on the surface and a portion of brown rust are observed at the later stage of the drying period (Figure 2.9 (e)). The specimen is covered with rust during the dry period. A small increase in the area of black rust and no big changes in the amount of corrosion products are observed using the endoscope (Figure 2.9 (f)). This result indicates that the corrosion reaction proceeds slowly during the dry period.

With the increase in RH during the wetting period, the surface of corrosion products begins to be moist. A small amount of corrosion products spreads out near the iron rust produced at the previous stages (Figure 2.9 (g)). The current shows a rapid decrease during the wetting

period even though the corrosion reaction is carried out on the steel surface. This result indicates that the decrease in the hydrogen evolution on the surface and the diffusion in steels are attributed to decreasing temperature. The amount of corrosion product shows a gradual increase on the steel surface during the 12 cycles (Figure 2.9 (h-n)). The results show that an amount of black iron rust accumulates along the perimeter of the rust circle and a portion of rust is generated near the boundary of the previous rust.

Figure 2.10 shows the optical microscope images of corroded surfaces of specimens after 12 wet/dry cycles. When the RH at the dry period is controlled above 60%, the amount of corrosion products is larger than the conditions under a lower RH. This result indicates that the amount of permeated hydrogen is related to the corrosion reaction. A notable orange rust ring can be observed on each specimen surface. When the RH at the dry period is higher than 55%, a large amount of black iron rust accumulates in the centre and perimeter of the ring.

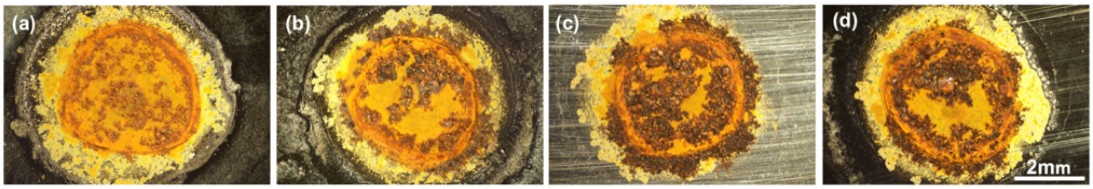

Figure 2.10. Optical microscope images of corroded surface after wet/dry cyclic corrosion tests with different RH values (a) 20%, (b) 55%, (c) 60% and (d) 65% in the dry period.

2.4 Discussion

2.4.1 Mechanism of hydrogen absorption reaction on the steel surface

At the initial stage, the corrosion process is carried out on the steel surface due to the presence of the droplet containing NaCl. The corrosion under droplet is an electrochemical

process by balancing anodic and cathodic reactions as shown in Figure 2.11. The area adjacent to the edge of the droplet provides easy access for oxygen to reach the steel surface and plays the role of the cathode with the reaction of oxygen reduction (Eq. (2.1)). The Fe^{2+} generated at the anodic site migrates into the cathodic site to form iron rust with OH^- generated by the oxygen reduction reaction (Eq. (2.2)). In addition, the Fe^{2+} derived from $Fe(OH)_2$ will be oxidized to $Fe(OH)_3$ by the dissolved oxygen (Eq. (2.3)).

$$O_2 + 2H_2O + 4e^- \rightarrow 4OH^- \quad (2.1)$$

$$Fe^{2+} + 2OH^- \rightarrow Fe(OH)_2 \quad (2.2)$$

$$Fe^{2+} + 2OH^- + (1/4)O_2 + (1/2)H_2O \rightarrow Fe(OH)_3 \quad (2.3)$$

The area under the center of the droplet functions as an anode due to the less access to oxygen. The anode serves as the corrosion initiation site and accelerates the dissolution of iron (Eq. (2.4)). The Cl^- contained in the droplet migrates to the anodic site to balance the positive charge of Fe^{2+} (Eq. (2.5)). $Fe(OH)_2$ is produced at the anodic sites due to the weak hydrolysis of the dissolved Fe^{2+} (Eq. (2.6)).

$$Fe \rightarrow Fe^{2+} + 2e^- \quad (2.4)$$

$$Fe^{2+} + Cl^- \rightarrow FeCl_2 \quad (2.5)$$

$$Fe^{2+} + 2H_2O \rightarrow Fe(OH)_2 + 2H^+ \quad (2.6)$$

Due to the presence of Cl^- in the solution layer, the oxidation reaction of Fe^{2+} to Fe^{3+} and the hydrolysis of the formed Fe^{3+} are accelerated to produce a considerable amount of hydrogen ions (Eq. (2.7)).

$$2Fe^{2+} + (1/2)O_2 + 5H_2O \rightarrow 2Fe(OH)_3 + 4H^+ \quad (2.7)$$

Hydrogen ion generated by the corrosion reaction is oxidized into atomic hydrogen which is

adsorbed on the steel surface. After adsorption, a small portion of adsorbed atomic hydrogen is absorbed by the steel as the hydrogen absorption reaction (Eq. (2.8)).

$$H_{ad} \rightarrow H_{ab} \tag{2.8}$$

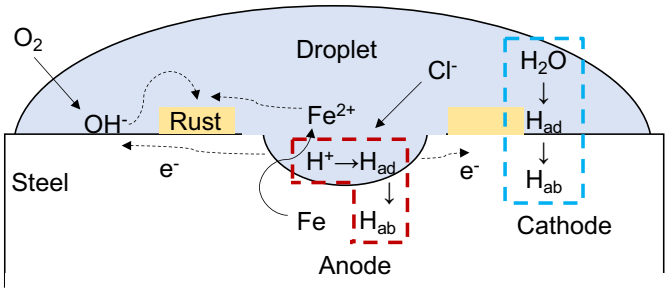

Figure 2.11. Schematic representation of the corrosion process combined with hydrogen adsorption and absorption reactions under a droplet.

2.4.2 Hydrogen permeation of steel during corrosion under low RH

As the evaporation of water on the steel surface during the drying period, the concentration of Cl^- contained in the solution layer increases, which is considered to accelerate the corrosion reactions and the evolution of hydrogen. Thus, the rapid increase in hydrogen permeation current during the drying period is attributed to the increasing concentration of Cl^-. After the drying period, temperature and RH are constant. The corrosion reaction with hydrogen evolution is inhibited due to the shrinking volume of the solution layer on the steel surface. The hydrogen permeation currents, therefore, begin to decrease during the dry period. This is the reason why the peaks can be observed at the beginning of dry periods (Figure 2.6).

The presence of NaCl particles in the rust layers plays a crucial role in the corrosion process during the dry period. NaCl particles possibly are moist and form thin electrolyte layers

at the interface between rust and steel substrate, considering that the capillary cohesion of water molecules may be increased by the corrosion products [9]. Figure 2.12 shows the schematic representation of the corrosion processes at the period of lower RH than DRH of NaCl. When the RH is kept higher than 55%, a portion of NaCl particles may deliquesce to form thin electrolyte layers under the rust. The electrolyte anions Cl^- migrate to the anodic site and balance the positive charge of dissolved Fe^{2+}. The electrolyte cations Na^+ migrate to the cathodic site and balance the negative charge of OH^-. Electric neutrality is maintained, and corrosion reaction proceeds at the dry period.

During the dry period, the rust on the steel surface is considered to be dehydrated due to the low RH, resulting in cracks in the rust layer. These cracks provide the routes for oxygen to reach the steel surface. Therefore, the Fe^{2+} formed in the anode areas can be oxidized by the oxygen (Eq. (2.7)). The accumulation of H^+ generated in the anodic site (Eqs. (2.6 and 2.7)) enhances the hydrogen evolution reaction and contributes to the increase in the current during dry periods in some cycles. As the corrosion reaction proceeds, the generated corrosion products are expected to block the entry of oxygen as well as the migration of ions between the cathodic and anodic sites, the current decreases due to the suppression of the hydrogen evolution and corrosion reaction. These phenomena on current are represented as the hump shape on the shoulder of the current curve at the dry period (Figure 2.6).

2.4.3 The effect of RH on the hydrogen absorption behaviour of steel

The distinct difference in hydrogen absorption activity under controlled RH from 20% to 65% is supposed to be due to the changes in the volume of dissolved NaCl inside the rust layer,

as shown in Figure 2.12. When the RH is controlled at 20%, the NaCl particle is difficult to absorb water and deliquesce into a liquid phase. There is almost no available electrolyte for the corrosion reaction on the steel surface. When the RH is above 55%, the significant acceleration of the hydrogen absorption activity suggests that there may be deliquesced NaCl particles inside the corrosion product. The state of the NaCl particle inside the corrosion product is supposed to be a solid-liquid phase at 55% RH. The volume of the solution layer increases with increasing RH, and more cathodic areas can be connected to enhance the corrosion reaction as well as the hydrogen evolution reaction.

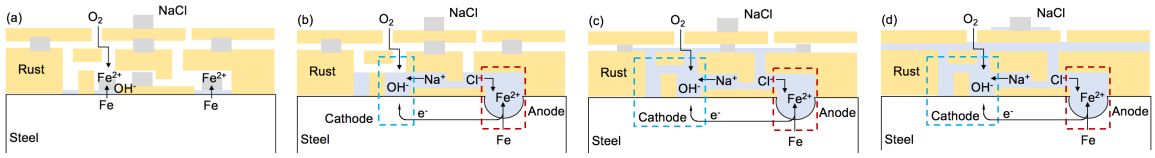

Figure 2.12. Schematic representation of the corrosion process under (a) 20% RH, (b) 55% RH, (c) 60% RH and (d) 65% RH.

After several cycles, the corrosion reactions are inhibited, and the hydrogen uptake tends to keep at a steady decrease when the RH is above 55%. It is a possible reason that the migration of ions between anodic and cathodic sites is obstructed, which is attributed to the accumulation of corrosion products. In the case of 20% RH, the amount of the corrosion product on the steel is smaller than in the other three conditions, which causes more oxygen to pass through the corrosion product and reach the steel surface for the corrosion reaction. As the corrosion reaction proceeds, the hydrogen evolution reaction can be accelerated by the gradual accumulation of Cl^- in the corrosion area, resulting in a slight acceleration of hydrogen entry

into steel during the dry period.

2.5 Conclusions

In this chapter, steel with an initial deposition of NaCl droplet was used to investigate the hydrogen permeation behaviour under different RH controlled below the DRH of NaCl during the dry periods. The effect of RH on the hydrogen permeation behaviour of steels was studied by hydrogen permeation tests under wet/dry corrosion environments. Optical techniques were used to understand the corrosion process of steel under the electrolyte layer. Based on the results, the following conclusions could be drawn:

- Hydrogen absorption into steel can occur even if the surrounding RH is below the DRH of NaCl. This process can be inhibited by the accumulation of corrosion products and much lower RH.
- The amount of permeated hydrogen increases with higher RH of the dry stage during the wet-dry cycles, which is attributed to the prolonged period of the presence of liquid phase inside the corrosion product.
- The changes in permeation current can be explained in terms of the state of NaCl inside the corrosion product. The NaCl particle is supposed to be a solid phase at 20% RH, a liquid-solid phase at 55% RH, and a liquid-rich phase above 60% RH.

A part of the work presented in this chapter has been reported in the publication:

Xiaole Han, Masatoshi Sakairi. Hydrogen permeation behavior of steel under wet/dry

corrosion with changes in relative humidity at the dry period, ISIJ International, 61 (2021) 1194-1200.

References

[1] S.T. Martin, Phase transitions of aqueous atmospheric particles. Chem Rev. 100 (2000) 3403-3454.

[2] T. Omura, T. Kudo, S. Fujimoto, Environmental factors affecting hydrogen entry into high strength steel due to atmospheric corrosion. Mater. Trans. 47 (2006) 2956-2962.

[3] E. Schindelholz, B.E. Risteen, R.G. Kelly, Effect of relative humidity on corrosion of steel under sea salt aerosol proxies: II. MgCl2, artificial seawater, J. Electrochem. Soc. 161 (2014) C460-C470.

[4] Y. Wang, J. Yamanishi, T. Haruna, Effect of Humidity of Air on Hydrogen Absorption into Fe with Rust Layer Containing MgCl2 during Atmospheric Corrosion, ISIJ Int. 61(2021) 1143-1150.

[5] E. Schindelholz, B.E. Risteen, R.G. Kelly, Effect of relative humidity on corrosion of steel under sea salt aerosol proxies: I. NaCl, J. Electrochem. Soc. 161 (2014) C450-C459.

[6] T. Haruna, Y. Shoji, Y. Hirohata, Hydrogen Absorption Rate into Fe with Rust Layer Containing NaCl during Atmospheric Corrosion in Humidity-controlled Air. ISIJ Int. 61 (2021) 1079-1084.

[7] T. Kushida, Hydrogen entry into steel by atmospheric corrosion, ISIJ Int. 43 (2003) 470-474.

[8] M.A.V. Devanathan, Z. Stachurski, The adsorption and diffusion of electrolytic hydrogen in palladium, Proc. R. Soc. Lond. Ser. A 270 (1962) 90-102.

[9] C. Li, Y. Ma, Y. Li, F. Wang, EIS monitoring study of atmospheric corrosion under variable relative humidity. Corros. Sci. 52 (2010) 3677-3686.

3 Role of Metal Cations in Hydrogen Absorption under Droplets

3.1 Introduction

Steel products used in atmospheric environments are susceptible to corrosion damage as natural phenomena like rain, dew, or fog can introduce water layers to the exposed steel surface. These liquid layers are usually dispersed on the metal surface in the form of droplets. When the atmospheric aerosols contain corrosive species such as NaCl and $MgCl_2$ in the marine environments, the dissolved chloride ion in the droplets is a well-known aggressive media and can cause localized passive film breakdown and accelerated corrosion of steel [1].

Zn-Al-Mg containing protective coatings are commonly employed to protect steel against corrosion attack. As corrosion proceeds under the droplets, metal cations like Zn^{2+}, Al^{3+} and Mg^{2+} from the anodic dissolution of coatings can participate in the corrosion process and significantly influence the corrosion kinetics [2] [3] [4] [5] [6]. Regarding the corrosion process of steel under salt deposits, the anodic iron dissolution and cathodic oxygen reduction reaction (ORR) are expected to produce a pH gradient in the electrolyte film [7]. The higher concentration of OH^- in the cathodic area is favourable for the migration of dissolved metal cations, resulting in the formation of precipitates that block the cathodic sites [8] [9] [10] [11]. Moreover, the dissolved metal cations have been shown to incorporate into the oxide films and exhibit different abilities to protect the metal from corrosion [12] [13] [14] [15] [16]. Although the retardation of the corrosion process by the dissolved metal cations is expected to hinder the hydrogen uptake of steel, various cations have been reported to enhance the hydrogen evolution reaction (HER) [17] [18] [19].

Accompanying the anodic metal dissolution, a proportion of dissolved metal cations can

hydrolyse and cause localized acidification [20], which is increasingly considered a prominent source of absorbed hydrogen into metals [21] [22] [23]. Regarding the metal cations dissolved from the protective coatings, it has been reported that Mg^{2+} and Zn^{2+} can participate during the corrosion processes and affect the corrosion kinetics [9] [10]. Liu et al. [17] reported that Al^{3+} had an acceleration effect on HER by facilitating the transport of the proton through the Al oxide/hydroxide film precipitated on the substrate surface. These results imply the significant role of Al^{3+} in hydrogen evolution during the corrosion process. The considerable influences of these cations on the corrosion processes make it critical to investigate their role in hydrogen entry into steel during atmospheric corrosion.

As metal cations can be quantitatively classified according to their acid strengths, the Hard and Soft Acids and Bases (HSAB) concept [24] has been introduced to explain the effects of metal cations on corrosion kinetics [25] [26] [27] [28]. Misono et al. [29] [30] proposed a dual parameter equation for metal ions to predict the stability of metal-ion complexes as follows:

$$\log K = \alpha X + \beta Y + \gamma \tag{3.1}$$

where K is the stability constant, X and Y are the dual parameters for the acids and are related to hardness and softness, respectively, α and β are the parameters for the bases, and γ is a constant determined for each base. The parameter X is regarded as cation hardness and is derived from Eq. (3.2):

$$X = {x_i}^2/10 \tag{3.2}$$

where x_i is the electronegativity of the metal cation. Table 1 lists the parameter X of each metal cation of interest from the literature [29]. Based on Eq. (3.1), some researchers reported that the corrosion rate was inhibited with the increase of parameter X of the metal cations in

the electrolytes [16] [28]. A reasonable mechanism is that a harder metal cation has a stronger affinity to be incorporated into the passive film that contains extensive hydroxide and bond water [25] [26] [31], and their corporation protects the metal from chloride ions [28]. However, their work was performed in bulk electrolyte environments, and the applicability of the HSAB concept in cyclic wet-dry environments remains to be demonstrated.

Table 3.1. Summary of the parameter X of the preferred metal cations.

Salt	Cation	Parameter X [29]
NaCl	Na^+	1.01
$MgCl_2 \cdot 6H_2O$	Mg^{2+}	3.54
$AlCl_3 \cdot 6H_2O$	Al^{3+}	7.70
$ZnCl_2$	Zn^{2+}	4.64

The work in this chapter aimed to investigate the role of dissolved metal cations in corrosion and hydrogen entry into steel under salt droplets. The difference in parameter X corresponding to the cation hardness of the salts provides a feasible way to examine the applicability of and HSAB concepts in explaining the role of cations in the corrosion process.

3.2 Experimental

3.2.1 Sample and salt solution

The sample was as same as the material used in Chapter 2. The surfaces of the steel samples were mechanically ground up to 2400 grit using silicon carbide papers. The polished samples were cleaned ultrasonically with ethanol and ultrapure water for 300 s, respectively, and then dried with flowing air before the tests.

The chloride salts of interest in the present chapter were NaCl, $MgCl_2$, $AlCl_3$, and $ZnCl_2$. The salt solutions were prepared using analytic grade reagents and ultrapure water at room temperature, as listed in Table 3.2. Since chloride ion is a well-known aggressive anion and has a significant influence on corrosion performance, the concentration of chloride ion in each salt droplet was controlled at 10 mM in order to compare the effects of metal cations on corrosion. Mixed salt solutions were prepared using aqueous NaCl and other salt solutions. Moreover, the presence of Al^{3+} presents a significant effect on the solution pH; therefore, the droplets containing Al^{3+} were divided as an independent group in the following tests.

Table 3.2. Salt solutions to initiate corrosion in the experiments.

Solution	Composition	pH
Group 1		
1	10 mM NaCl	5.9
2	5 mM $MgCl_2 \cdot 6H_2O$	5.8
3	3 mM $MgCl_2 \cdot 6H_2O$ + 4 mM NaCl	5.7
4	5 mM $ZnCl_2$	5.7
5	3 mM $ZnCl_2$ + 4 mM NaCl	5.7
Group 2		
1	3.3 mM $AlCl_3 \cdot 6H_2O$	4.0
2	2.5 mM $AlCl_3 \cdot 6H_2O$ + 2.5 mM NaCl	4.1
3	1 mM $AlCl_3 \cdot 6H_2O$ + 7 mM NaCl	4.3
4	10 mM NaCl	5.8

3.2.2 Hydrogen permeation and cyclic corrosion tests

Figure 3.1 show the Schematic drawing of the experimental procedures. An

electrochemical setup consisting of an upper exposed area for corrosion occurrence and a lower electrochemical cell for hydrogen detection was employed to detect the atomic hydrogen that diffused through the samples during cyclic corrosion. The details of the hydrogen permeation detection cell have been introduced in Chapter 2. One side of the sample was electroplated with Ni layer and was attached to the hydrogen detection cell, acting as the working electrode (WE). The counter and reference electrodes (CE and RE) were made of Pt wires, and the electrolyte was 1 M NaOH solution. The sample was polarized at a constant anodic potential of -30 mV vs. Pt using a potentiostat. This potential was sufficient to ensure rapid ionization of the atomic hydrogen that diffused through the sample. The changes in the anodic current of the detection cell were recorded during the cyclic corrosion test. In addition, the background current was recorded without performing corrosion upon the sample and subtracted from the detected hydrogen permeation currents to eliminate the interference of temperature on the anodic current fluctuation.

After the sample was assembled with the hydrogen detection cell, the upper side of the sample was performed as the corrosion side and exposed to a controlled cyclic wet-dry environment. The temperature and humidity inside the chamber were controlled according to a pre-designed procedure. Considering the DRH and ERH values of the salts, the RH variation was set from 90% to 20% to achieve the wet-dry conditions. The design of the variation of temperature was intended to keep the environment at a constant dew point of 25˚C. However, the temperature interval in the experiments was narrowed to 30˚C to 50˚C to avoid current noise caused by excessive temperature changes in the hydrogen detection cell. The changes in temperature and humidity consist of four stages: wet (1 h), drying (1 h), dry (3 h), and wetting

(1 h) to the initial wet condition.

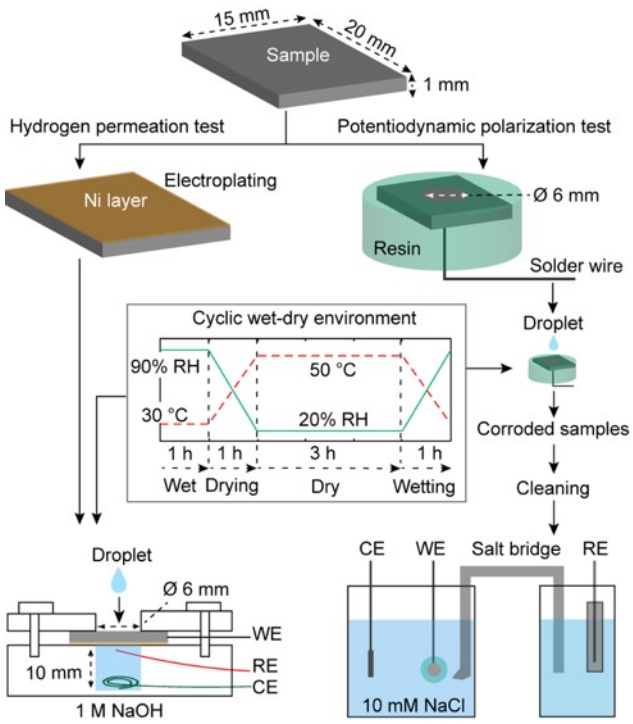

Figure. 3.1 Schematic drawing of the experimental procedures.

3.2.3 Potentiodynamic polarization test

The potentiodynamic polarization data of the samples at various stages of a wet-dry corrosion cycle were of interest in the present work, including the as-polished sample, and the corroded samples after the wet (1 h) and drying (1 h) stages under aqueous salt droplets (10 mM NaCl and 3.33 mM $AlCl_3$), respectively. The samples were mounted in resin with an exposure area of 28.3 mm^2 for droplet deposition. After the corrosion tests under corresponding conditions, the polarization curves of the samples were measured in a three-electrode electrochemical cell with the samples as WE, a platinum plate (2cm × 2cm) as CE, and an Ag/AgCl electrode (SSE) immersed in a saturated KCl solution as RE. Note that the corroded

surfaces were cleaned using ultrapure water to remove the residual droplets before the electrochemical measurements. The measurements were carried out in 10 mM NaCl solution and performed using a potentiostat (PocketSTAT, Ivium Technologies, Netherlands). After the measurement of open-circuit potential for 1 h at room temperature, the potential scan was performed at a rate of 1 mV/s in the cathodic and anodic directions to obtain individual polarization curves.

3.2.4 Surface characterisation and analysis

The changes in the surface morphology of the samples during the cyclic corrosion process were recorded using a USB camera connected to a personal computer. Micrographs of the corroded surface were taken using an optical microscope. An X-ray photoelectron spectroscope (XPS, JPS-9200, JEOL Ltd., Japan) with an Mg Kα X-ray source was used to identify the elements and their chemical states in the sample surfaces. The samples used for XPS analysis were ultrasonically cleaned in purified water for 300 s to remove the residual corrosion products on the surfaces. The analysis area was a 3 mm diameter region centred on the corrosion zone. The curve fitting procedures were conducted in CasaXPS software and the adventitious carbon peak at 284.8 eV was used for charge correction.

3.3 Results

3.3.1 Corrosion morphology under salt droplets

3.3.1.1 Corrosion morphology under NaCl, $MgCl_2$, and $ZnCl_2$ droplets

Figure 3.2 presents a series of optical images showing the surface changes of the samples

during the initial wet-dry stage, which are selected from a time-lapse video that records the surface changes of the samples during the initial three cycles (The video is available online and can be found at doi:10.1016/j.corsci.2024.111993). The deposited droplets have approximately the same size and shape at the beginning of the corrosion tests. After the start of the wet-dry cycle, corrosion occurs rapidly on the samples under the droplets containing Na^{+} and Mg^{2+}. Yellow flocculent corrosion products appear on the surfaces after 10 min and relatively black regions can be observed near the central areas of the samples (Figure 3.2 (a) and (b), indicated by white arrows). These black areas indicate the initiation of anodic dissolution of iron.

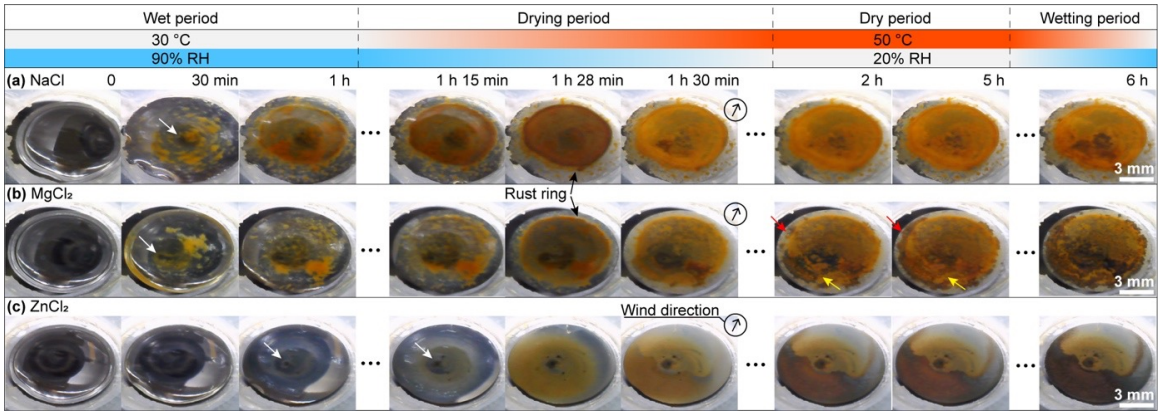

Figure 3.2. Optical images of sample surface changes during the first cycle under (a) 10 mM NaCl, (b) 5 mM $MgCl_2$, and (c) 5 mM $ZnCl_2$.

After one hour, the area covered by yellow corrosion products under the NaCl droplet is greater than that under $MgCl_2$, and the products tend to precipitate in the region between the centre and edge of the droplets. In the case of the Zn^{2+}-containing droplet, no visible corrosion products can be observed in the first hour until the appearance of a black spot (Figure 3.2 (c), white arrow) in the central area, surrounded by a slight white layer. These observations demonstrate that the corrosion process is most active under the NaCl and $MgCl_2$ droplets and

is greatly inhibited when the droplet contains Zn^{2+}.

As the RH decreases from 90% to 20% and droplets begin to evaporate in the drying period, the amount of rust on the samples under NaCl and $MgCl_2$ droplets increases, and ring-shaped rust layers can be found along the peripheral regions of the droplets (Figure 3.2 (a) and (b), black arrows), leaving white layers at the outermost peripheries. About halfway through the drying period, a distinct transition of the surfaces from visible wet to dry appears on all the samples (Figure 3.2). The white layers formed under NaCl extend almost to the edge of the exposed surface, whereas those under $MgCl_2$ are along the initial droplet rim. Remarkably, the surface morphology of the sample under $ZnCl_2$ presents a particular phenomenon. As shown in Figure 3.2 (c), a yellow rust layer gradually forms around the initial black spot instead of large amounts of flocculent corrosion products. In addition, the yellow layer prefers to form towards one side of the peripheral region, leaving a visible uncorroded area covered by a white film. This phenomenon is related to the influence of airflow inside the chamber. According to the wind direction as shown in Figure 3.2, the windward side of the sample surfaces becomes dry more quickly than the leeward side. The faster airflow and higher oxygen content on the windward side may be the reason for the formation of white films. The composition of these surface films will be investigated in the following section.

In the dry period, the RH is steady at 20% which is lower than the ERH of NaCl but higher than that of $MgCl_2$ and $ZnCl_2$. In the case of the sample under the $MgCl_2$ deposition, it is apparent that new corrosion products are present on the previous white layers along peripheral regions of the rust ring (Figure 3.2 (b)). Additionally, the previous black corrosion products

turn brown in the dry period (Figure 3.2 (b), yellow arrows). As demonstrated in the literature [32], the colour change of the corrosion products is probably related to the oxidation of black magnetite to brown rust by oxygen.

By contrast, no perceptible development of the corrosion products under the other salt depositions can be observed from optical observations. These phenomena suggest that the $MgCl_2$ deposition allows for the corrosion process to continue even under low humidity, while the $ZnCl_2$ deposition, which can absorb moisture more easily than $MgCl_2$, has no promotion effect on corrosion. When the RH increases from 20% to 90%, appreciable amounts of new black corrosion products appear on the rust layers during the second half of the wetting period (Figure 3.2). According to the well-accepted mechanism of atmospheric rusting of iron [32], the conversion of brown rust layers to black magnetite takes place accompanied by the anodic dissolution of iron in the presence of water. Therefore, the colour change indicates active corrosion processes when the surfaces become wet again.

3.3.1.2 Corrosion morphology under salt droplets with varying Al^{3+} concentrations

After the deposition of salt droplets containing Al^{3+}, two typical changes in the corrosion morphology of samples are displayed in Figure 3.3, selected for exposure to (a) a mixed salt solution (1 mM $AlCl_3$ + 7 mM NaCl) and (b) 3.33 mM $AlCl_3$. The deposited salt solutions have apparent droplet shapes at the beginning of the corrosion test. Within half an hour after the initiation of the wet-dry process, no perceptible corrosion products appear on the sample surfaces, and the droplets tend to spread outward and cover the exposed surfaces. At the end of the wet period (1 h), considerable amounts of yellow corrosion products develop and

accumulate along the peripheral region of the NaCl-containing droplet, forming a ring-shaped rust layer (Figure 3.3 (a), white arrow).

On the other hand, the corrosion morphology under the droplet containing 3.33 mM $AlCl_3$ exhibits a distinct difference from the droplet containing NaCl. An appreciable black spot (Figure 3.3 (b), white arrow) exists in the central area in preference to the formation of an apparent rust ring in the peripheral area of the droplet. Considering the oxygen concentration difference in the droplet, the central spot is supposed to be the anodic region. Al^{3+} is expected to migrate to the peripheral cathodic region and precipitate within an appropriate pH range, forming a slight white layer on the sample surface (Figure 3.3 (b), red arrow) instead of abundant yellow corrosion products observed under the NaCl-containing droplet. This precipitated white layer has been shown to accelerate HER in the cathodic region [17], which is expected to facilitate hydrogen entry into steel when the corrosion proceeds under the $AlCl_3$ droplet.

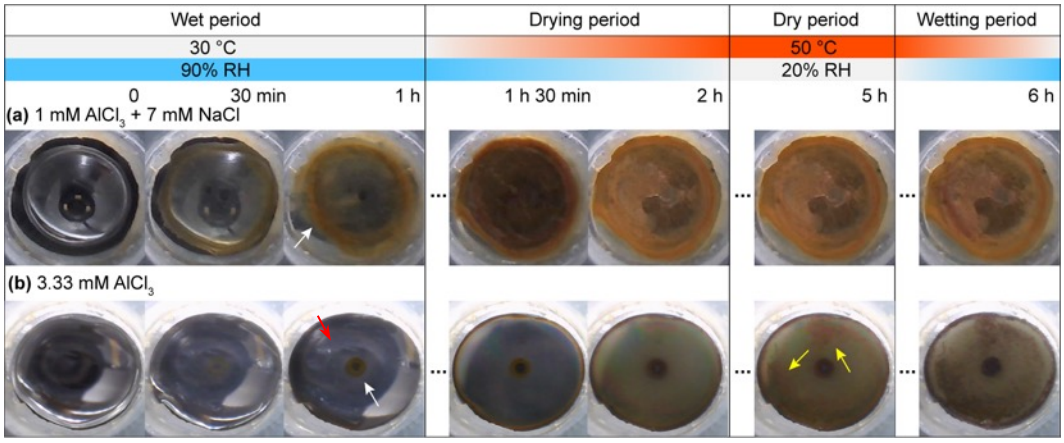

Figure 3.3. Optical images of corrosion morphology of the samples under (a) 1 mM $AlCl_3$ + 7 mM NaCl and (b) 3.33 mM $AlCl_3$ during cyclic corrosion.

In the subsequent drying period, the amounts of corrosion products under the NaCl-containing droplet increase as water evaporates. However, the changes in surface morphology under the $AlCl_3$ droplet are apparently different from the NaCl-containing droplet, manifested by no appreciable change in the amounts and colour of the corrosion products. The increase in the concentration of Al^{3+} retards the formation of corrosion products under the droplet. Combining the results of the hydrogen permeation tests, the increase in the concentration of Al^{3+} accelerates hydrogen entry regardless of the amounts of corrosion products during the corrosion processes.

After the droplets evaporate, the sample surfaces become visibly dry, and the corrosion processes are supposed to be hindered by the absence of electrolyte layers. However, new corrosion products can be found along the peripheral regions of the exposed surface (Figure 3.3 (b), yellow arrows). Although 20% RH is much lower than the DRH of $AlCl_3$ particles and no electrolyte is expected, corrosion can still proceed under the rust layers. As the RH increases and temperature decreases to the wet conditions, noticeable new corrosion products can be found on the sample under the $AlCl_3$ droplet.

3.3.2 Hydrogen permeation current under salt droplets

3.3.2.1 Hydrogen permeation current of samples under NaCl, $MgCl_2$, and $ZnCl_2$ droplets

Figure 3.4 (a) shows the records of the hydrogen permeation current densities corresponding to the wet-dry cycle of the corrosion processes (Figure 3.2). The current variation represents the instantaneous rate of hydrogen permeation through the samples. In the first wet period, the currents remain nearly unchanged before the droplets begin to evaporate.

This suggests that no appreciable hydrogen permeation occurs under the droplets, although an appreciable amount of corrosion products is formed on the samples under the NaCl and $MgCl_2$ droplets (Figure 3.2 (a) and (b)).

Afterwards, the currents show a pronounced increase in the drying period, indicating the production of a significant amount of diffused hydrogen with increasing temperature and decreasing RH. It is noteworthy that the current of the sample under the $ZnCl_2$ droplet initiates a prompt increase after a noticeable delay compared with the other two conditions. The delayed current increase indicates the inhibition of Zn^{2+} on the hydrogen absorption activity before droplet drying. On the other hand, the current under $ZnCl_2$ shows the most significant increase than other salts, suggesting the acceleration effect of $ZnCl_2$ on hydrogen absorption during the drying period.

After the beginning of the dry stage, the currents begin to decline after reaching a maximum value. The appearance of the decay transient indicates the retardation or stagnation of the hydrogen entry into samples. Significantly, the current of the sample exposed to the $MgCl_2$ deposition exhibits a diminished decline and remains at high values at the end of the dry period. This particular phenomenon reveals that although the corrosion reaction is supposed to be hindered due to the lack of electrolytes under dry conditions, the hydrogen absorption reactions remain active at the entry surface. Corresponding to the corrosion morphology in the dry period shown in Figure 3.2 (b), the proceeding of the corrosion processes under the $MgCl_2$ deposition is responsible for providing the hydrogen source.

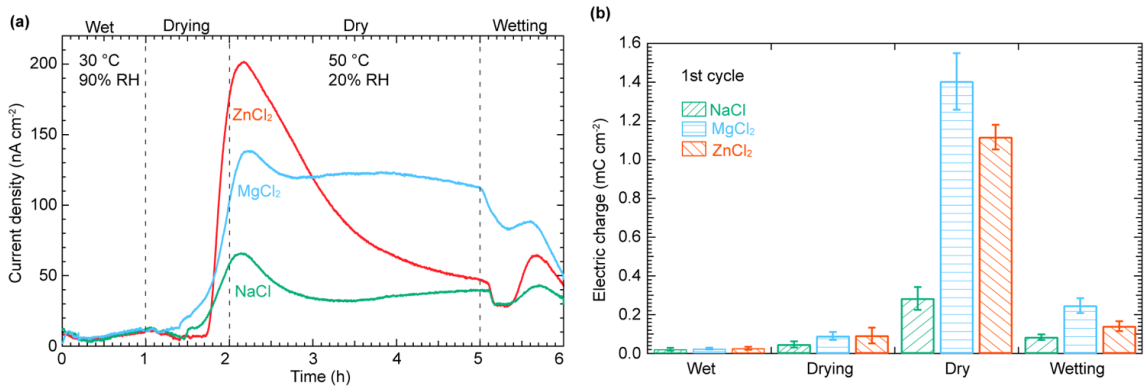

Figure 3.4. (a) Changes in hydrogen permeation current densities of the samples exposed to salt droplets during the first cycle. (b) Electric charges of the samples during each stage of the first cycle. Error bars represent standard deviation.

In the final wetting period, the current curves present an initial quick decline due to the decrease in temperature. Subsequently, the curves exhibit a camel-shaped change with increasing RH. According to the surface observations, the current rises occur earlier than the appearance of large amounts of black corrosion products. This phenomenon indicates that a higher RH contributes to the corrosion process without accelerating hydrogen entry into steel. As the deposited salts absorb moisture with increasing RH, the acceleration of hydrogen absorption is considered to be attributed to the initial thin electrolyte layers rather than a larger volume of electrolytes. A higher concentration of corrosive ions within the rust layers may be necessary for hydrogen evolution and absorption reactions.

Figure 3.4 (b) shows the hydrogen contents by integrating the current densities of the samples under salt droplets during each period of the first wet-dry cycle. Combined with the changes in permeation currents in Figure 3.4(a), the quantitative analysis of the diffused hydrogen suggests that the initial drying to wetting periods predominate in the hydrogen entry into steel during the corrosion process under salt droplets. In other words, thin electrolyte layers

with high concentrations of aggressive ions play a dominant role in the hydrogen absorption reactions. Moreover, the quantity of diffused hydrogen through the samples under $MgCl_2$ and $ZnCl_2$ droplets is significantly larger than that under NaCl droplets, which suggests that the lower ERH and DRH values of salts extend the presence of electrolyte layer and contribute to the hydrogen uptake by samples. However, although $ZnCl_2$ has the strongest ability to absorb moisture and maintain the presence of electrolyte layers, the quantity of absorbed hydrogen under the $ZnCl_2$ deposition is lower than that under $MgCl_2$, which might be attributed to the inhibition effect of Zn^{2+} on the corrosion process of steel.

3.3.2.2 Hydrogen permeation current of samples under Al^{3+} containing droplets

Figure 3.5 shows a typical record of the hydrogen permeation current density of the sample exposed to 3.33 mM $AlCl_3$ droplet a wet-dry cycle (6 h). The current increases gradually during the initial wet period, implying the occurrence of hydrogen absorption into the sample. In the subsequent drying period, the current increases prominently as RH decreases and temperature increases, which indicates that the drying condition accelerates the hydrogen evolution and entry into steel during the corrosion process. When the environment is constant at a high temperature and a low RH, the current reaches a maximum value and then decreases at a rapid rate in the dry period. This phenomenon suggests the retardation of hydrogen absorption into the sample. In the final wetting period, the current declines initially due to the decrease in temperature, and then exhibits a hump-shaped change, indicating that the increase in RH facilitates the hydrogen entry process.

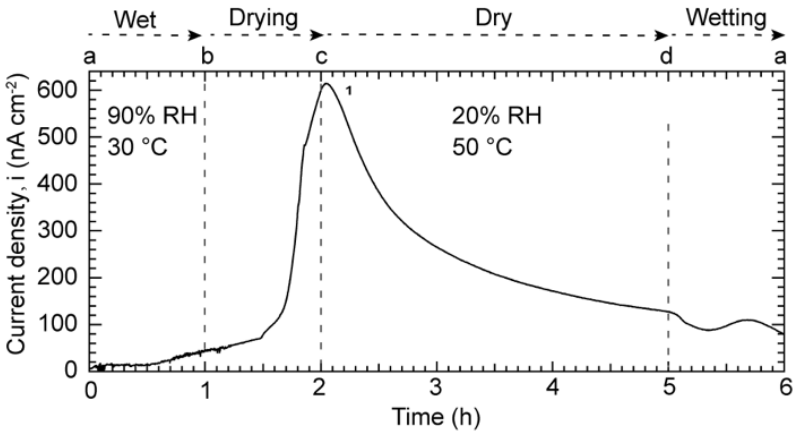

Figure 3.5. Typical change in hydrogen permeation current density of the sample exposed to the droplet of 3.33 mM $AlCl_3$ solution during the cyclic corrosion test.

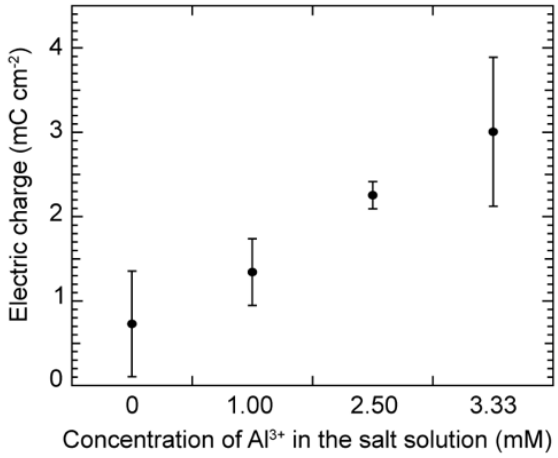

Figure 3.6. Comparison of electric charges of the samples during the wet-dry cycle. Error bars represent one standard deviation.

In an attempt to investigate the role of Al^{3+} in hydrogen entry into steel during cyclic corrosion, the present study examined the hydrogen permeation behaviour of the samples exposed to four kinds of salt droplets with varying Al^{3+} concentrations. As shown in Figure 3.6, the amount of permeated hydrogen is obtained by integrating the permeation current density with respect to the durations of wet-dry cycle. When the corrosion processes start and proceed under the initial salt droplets, hydrogen absorption and diffusion take place. The amount of

permeated hydrogen through the samples increases with increasing concentrations of Al^{3+}. The results suggest that the presence of Al^{3+} plays an important role in the hydrogen absorption process during the corrosion under the initial droplet. The higher the concentration of Al^{3+} in the droplet, the higher the activity of hydrogen absorption into steel.

3.3.3 Formation of Mg^{2+}/ Zn^{2+}-containing films under droplets

During each stage of the wet-dry cycle, the composition of salt droplets presents a significant effect on the corrosion morphology and the corresponding hydrogen absorption activity. To investigate the role of Na^{+}, Mg^{2+}, and Zn^{2+} in the rust formation during the drying of salt droplets, XPS analysis was performed on the sample surfaces during the initial wet-dry cycle. After the samples were corroded under salt droplets for 1 h, Mg 1s, auger Mg KLL, Zn $2p_{3/2}$, and auger Zn LMM peaks were detected in the wide-scan XPS spectra as shown in Figure 3.7. Since the samples were ultrasonically cleaned before XPS analysis, the results demonstrate that the metal cations, Mg^{2+} and Zn^{2+}, were incorporated into the surface films of steel during the corrosion process under salt droplets.

Regarding the composition of corrosion products, the narrow-scan XPS spectra of O 1s indicate that the surface layers are mainly composed of hydroxide and oxide (Figure 3.8). The peak of 284.8 eV is related to the C-C bonds, and the peaks around 286.5 eV and 288.6 eV can be attributed to C-O and O-C=O bonds in the C 1s spectra. The peaks of 530.0 eV and 531.4 eV correspond to the oxide and hydroxide bonds, and the third peak of about 532.4 eV may be associated with hydration water in the O 1s spectra [33]. Although the C 1s spectra suggest the presence of carbonates, the contribution of the C-O and O-C=O bonds to the O 1s spectra is

smaller than the oxide and hydroxide bonds.

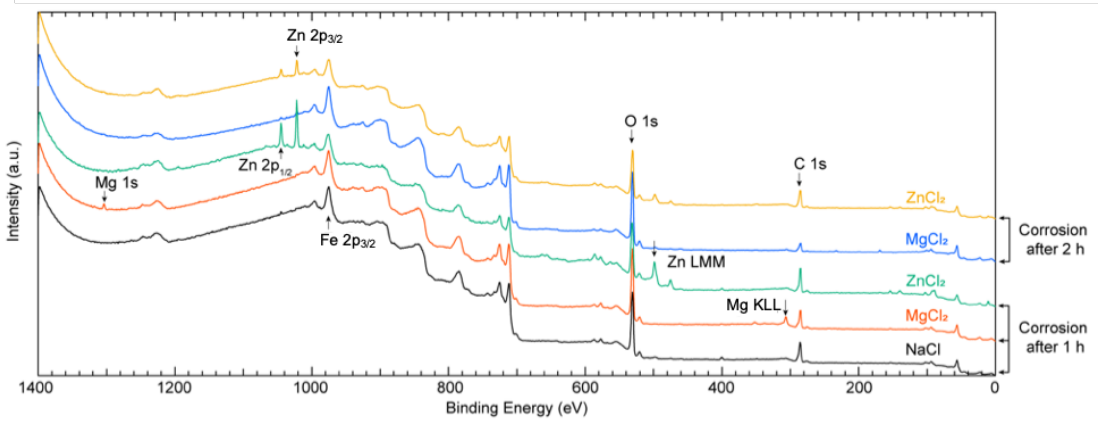

Figure 3.7. Wide-scan XPS spectra of the samples after corrosion for one and two hours in the first wet-dry cycle.

The XPS spectra of Mg 1s and Zn $2p_{3/2}$ shown in Figure 3.9 exhibit the chemical states of the metal cations on the sample surfaces. The binding energy of the Mg 1s peak can be fitted into two peaks centred at 1304.03 eV and 1303.27 eV, which are related to the binding energies of MgO and $Mg(OH)_2$, respectively [34]. The peak of Zn $2p_{3/2}$ is centred at 1021.47 eV and agrees with the binding energy of ZnO [35]. In the following drying period, water evaporation accelerates the formation of corrosion products at the sample surfaces. After the drying procedure, the samples were ultrasonically cleaned again in purified water before XPS analysis. As shown in Figure 3.7, Mg was not detected in the wide-scan XPS spectra after droplet drying (2 h). The MgO and $Mg(OH)_2$ films formed previously under $MgCl_2$ droplets are supposed to be destroyed by accelerated corrosion as water evaporates.

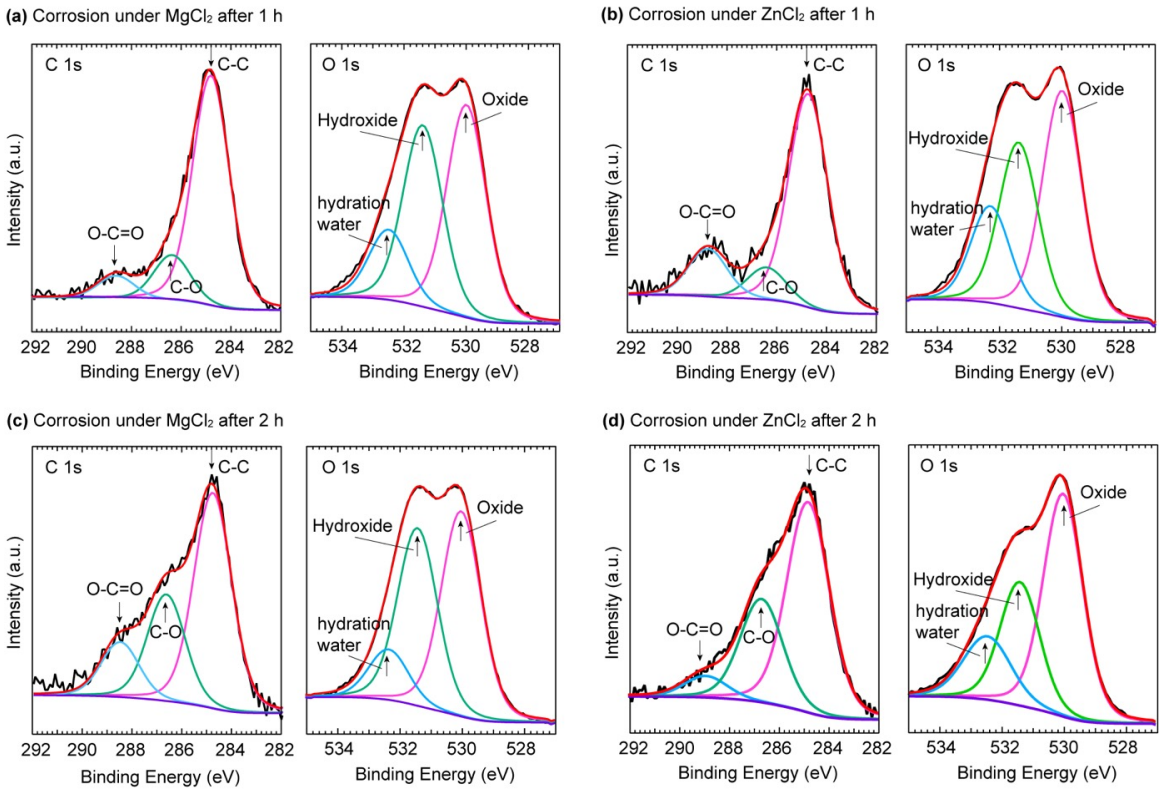

Figure 3.8. Narrow-scan XPS spectra of C 1s and O 1s of the samples after the first and second hours of corrosion under 5 mM $MgCl_2$ and 5 mM $ZnCl_2$ salt droplets.

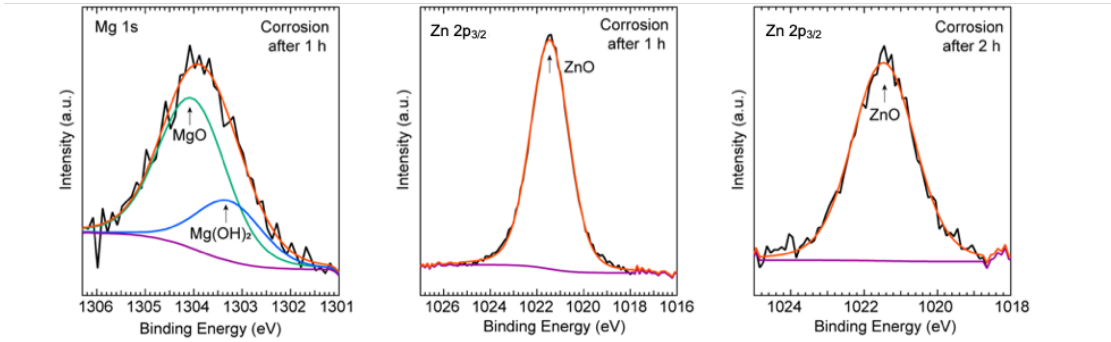

Figure 3.9. Narrow-scan XPS spectra of Mg 1s and Zn $2p_{3/2}$ of the samples after one hour and Zn $2p_{3/2}$ of the sample after two hours of corrosion.

On the other hand, the narrow-scan spectrum of Zn $2p_{3/2}$ presenting a peak of 1021.48 eV demonstrates the presence of Zn in the form of ZnO after droplet drying. The results suggest that metal cations such as Mg^{2+} and Zn^{2+} contribute to the formation of oxide and hydroxide

films on steel surfaces under salt droplets. Furthermore, the formation of ZnO significantly enhances the stability of the steel surfaces and makes the steel less susceptible to corrosion attack.

3.3.4 Electrochemical kinetics of steel under droplets with varying Al^{3+} concentrations

As the samples under droplets with varying Al^{3+} concentrations exhibited considerable discrepancy in the corrosion morphology and hydrogen permeation behaviour, this study measured the electrochemical kinetics of the samples at various stages of the first corrosion cycle, including the corroded samples after the drying stage (2 h) under (a) 3.33 mM $AlCl_3$ and (b) 10 mM NaCl, the corroded samples after the wet stage (1 h) under (c) 3.33 mM $AlCl_3$ and (d) 10 mM NaCl, and (e) the as-polished samples.

Figure 3.10 shows the polarization curves of the samples that were corroded under salt droplets after different stages of a wet-dry cycle. Prior to the electrochemical measurements, the corroded samples were cleaned with ultrapure water to remove the residual droplets and unconsolidated corrosion products. The cathodic kinetics of the samples at different stages display distinct differences in the diffusion-limited current densities (DLCD). DLCD for the samples corroded under 10 mM NaCl droplets is smaller than that under 3.33 mM $AlCl_3$ droplets after the same corrosion durations. Apart from the reduction reaction of dissolved oxygen in the electrolyte, the increase in the cathodic current density is suggested to be attributed to the reduction reactions of iron rust on the corroded surfaces, involving the conversion of FeOOH to Fe_3O_4:

$$3FeOOH + e^- \rightarrow Fe_3O_4 + H_2O + OH^- \quad (3.3)$$

Therefore, the larger amount of adherent iron rust on the sample surfaces might be responsible for the stronger cathodic kinetics of the samples in the polarization tests.

Although the amounts of corrosion products under NaCl-containing droplets are greater than that under $AlCl_3$ droplets, it should be noted that the corroded samples were cleaned with ultrapure water prior to the measurements. The corrosion products under NaCl droplets were unconsolidated on the sample surfaces and easily removed by ultrapure water. In contrast, the generated corrosion products under $AlCl_3$ droplets adhered tightly to the sample surfaces, contributing to the cathodic kinetics of the corroded samples in the polarization tests. These results demonstrate the positive role of Al^{3+} in the formation of adherent rust layers on steel during corrosion under salt droplets. Furthermore, DLCD for the samples corroded under salt droplets after the drying stage (2 h) is greater than that after the wet stage (1 h). The increase in the amounts of corrosion products after the drying stage is considered to be responsible for the increasing DLCD.

Another characteristic of the polarization curves is the difference in the corrosion potentials of the samples. The corrosion potential of the sample under (a) $AlCl_3$ after the drying stage is nobler than that under (b) NaCl, attributed to the suppression of anodic dissolution after the formation of precipitates on the sample under $AlCl_3$ droplets. This is consistent with the observation results that no prominent increase in the amounts of corrosion products appears on the sample surfaces. In summary, the polarization data demonstrate that the amount of adherent corrosion products under $AlCl_3$ is larger than that under NaCl, attributing to the precipitation of Al compounds. In addition, the Al-containing precipitated films are suggested to retard the initial dissolution of iron under $AlCl_3$ droplets. These results corroborate the findings that Al^{3+}

can introduce a precipitated layer on the steel, suppressing iron dissolution while accelerating hydrogen absorption during the corrosion of steel under $AlCl_3$ droplets.

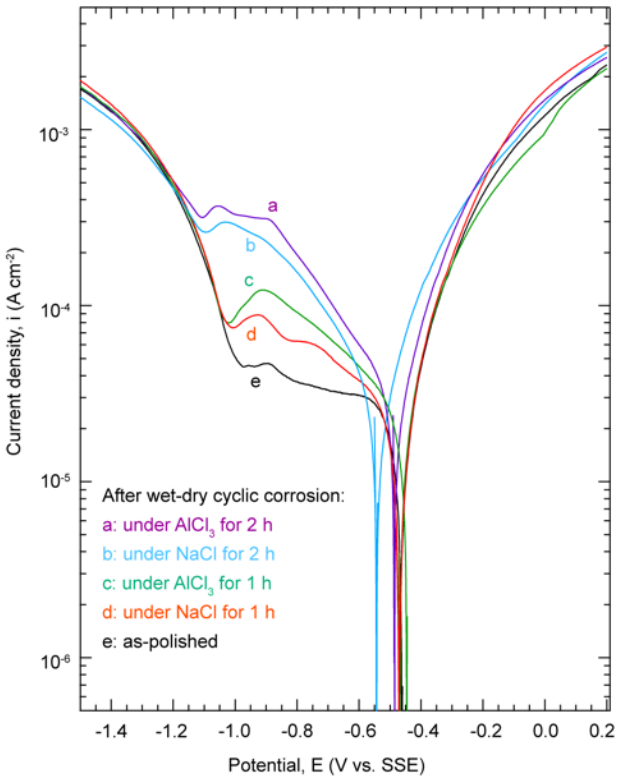

Figure 3.10. Polarization curves of the samples subjected to corrosion at different stages of the initial wet-dry cycle.

3.4 Discussion

3.4.1 Role of salts in corrosion and hydrogen absorption under droplets

When the corrosion takes place under salt droplets, the composition of the electrolytes has a distinct influence on the corrosion morphology, and no perceptible hydrogen entry occurs at this stage. To explain the corrosion process of steels under droplets, a well-known droplet model proposed by Evans provides insight into the effect of the oxygen concentration gradient in the droplet. The corrosion morphology observed in the present study generally follows this mechanism. The droplet shape facilitates the access of oxygen to the steel surface through the

edge of the droplet and thus establishes a concentration cell with the edge area acting as the cathode and the central area acting as the anode. Ferrous ions released from the anode migrate to the peripheral area and combine with hydroxide ions produced by the oxygen reduction reaction (ORR) to form rust. Therefore, the results of this study indicate that when corrosion occurs under salt droplets, the predominant reactions are anodic iron dissolution and cathodic ORR.

In this study, the metal cations of the salts present a different ability to form barrier layers to corrosion attack under droplets. As corrosion proceeds under salt droplets, Mg^{2+} and Zn^{2+} can introduce hydroxide/oxide components into the steel surfaces. In particular, the Zn^{2+}-containing films have a better corrosion resistance than Mg^{2+}-containing films and cannot be destroyed easily with corrosion proceeding. The corrosion morphology of steel under $AlCl_3$ droplet is similar to that under $ZnCl_2$, and the precipitated layers containing Al_2O_3 present an ability to retard iron dissolution before the droplet evaporates. Given that the hardness of metal cations decreases from Al^{3+} to Na^{+} as listed in Table 3.1, it is reasonable to assume that the metal cations with higher hardness contribute to the formation of protective films with higher corrosion resistance. The surface observations and XPS analysis demonstrate that the cation-combined protective films form at an early stage (less than 10 min after the deposition of salt droplets) before the formation of corrosion products. Accordingly, the improvement of corrosion resistance of surface layers is probably attributed to the formation of hydroxide/oxide films of harder metal cations such as Zn^{2+} on the top of the original passive films. Another reasonable mechanism is that the harder metal cations can bind to the passive films and repair the defects to improve corrosion resistance.

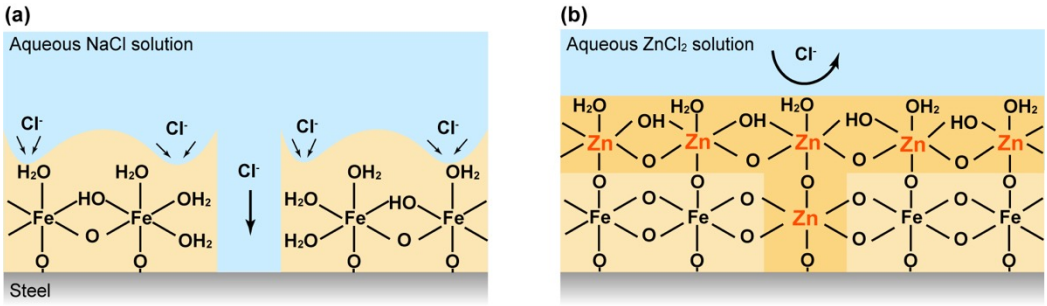

Figure 3.11. Proposed models of (a) the attack of chloride ions on the surfaces and defective sites of the passive film under aqueous NaCl solution, (b) the combination of Zn and passive film presenting a protective effect against corrosion

Based on a passive film model proposed by Okamoto et al. [31], the initial passive film on steel is supposed to be a hydrated oxide film under aqueous salt solutions, containing H_2O-Fe-OH_2, -HO-Fe-OH-, and -O-Fe-O- structures. As illustrated in Figure 3.11 (a), when the corrosion of steel takes place under an aqueous NaCl droplet, the chloride ions lead to the localized breakdown or migrate to defective sites of the passive films, accelerating the localized corrosion of the underlying steel. According to the HSAB concept, metal cations with higher hardness acting as hard acids prefer to bind to hard bases such as H_2O and OH^-. For this reason, harder metal cations such as Zn^{2+} and Al^{3+} are easier to combine with the hard bases of the passive film of steel. As illustrated in Figure 3.11 (b), Zn^{2+} in the electrolytes binds to the hydrated oxide on the top of the passive film or repairs the defective sites of the passive film, inhibiting the corrosion attack from chloride ions. In addition, the combination of metal cations and the passive films accelerates the deprotonation of the passive film and contributes to the formation of well-developed oxide films (-O-M-O-) [31]. As a result, harder metal cations such as Zn^{2+} and Al^{3+} introduce the formation of stable oxides such as ZnO and Al_2O_3, presenting an inhibition effect on the corrosion of steel under salt droplets.

The experimental results demonstrate the presence of hydrogen evolution and absorption during the cyclic corrosion of steel under salt droplets. Al^{3+} plays a significant role in the corrosion morphology and hydrogen entry into steel during the corrosion processes under the initial droplet and after the droplet evaporates.

3.4.2 Proposed models for hydrogen entry into steel under $AlCl_3$ droplet

The experimental results demonstrate that Al^{3+} plays a significant role in the corrosion morphology and hydrogen entry into steel during the corrosion processes under the initial droplet and after the droplet evaporates.

The corrosion process and hydrogen entry into steel under the $AlCl_3$ droplet is illustrated in Figure 3.12. Attributing to the droplet shape, oxygen is easy to reach the edge of the droplet and establishes a concentration cell in the droplet. An important feature of droplet corrosion is the migration of ions in the conductive electrolytes to maintain charge neutrality between the anodic and cathodic sites. Regarding the corrosion processes under the $AlCl_3$ droplet, Cl^- is expected to move towards the anodic site and accelerate the iron dissolution, while Al^{3+} migrates to the cathodic site where ORR is predominant. Unlike the NaCl droplet, where Na^+ is considered to maintain the local alkaline environment at the cathode, Al^{3+} tends to form precipitates and buffer the pH in the cathodic area. As a result, the changes in the local chemistry suppress ORR and enhance HER as the dominant cathodic reaction, which accelerates hydrogen absorption into steel.

On the other hand, the concentration of Cl^- is supposed to increase as water evaporates, which induces the breakdown of the Al-containing films and the development of new localized

corrosion sites on the steel surface. Accompanying the anodic dissolution, the hydrolysis of the released iron ions leads to a decrease in the pH in the anodic areas. As a result, the decrease in the pH of the local environments provides an increased driving force for HER assuming a constant corrosion potential, which has a promotion effect on hydrogen absorption into steel.

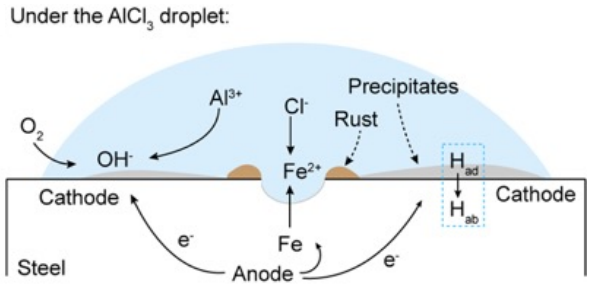

Figure 3.12. Schematic description of the corrosion process and hydrogen absorption into steel under the $AlCl_3$ droplet.

3.5 Conclusions

The present study examined the corrosion morphology and the associated hydrogen permeation behaviour of steel after the placement of salt solution droplets. Several conclusions can be drawn as follows:

- When corrosion occurs under salt droplets, Mg^{2+} and Zn^{2+}-containing surface layers are formed on the steel surfaces and the latter presents a high corrosion resistance. Based on the HSAB concept, the metal cations that have higher cation hardness, parameter X, are easier to combine with the hard bases such as H_2O and OH^- of the passive films, forming stable protective passive films against corrosion attack under salt droplets.
- The concentration of Al^{3+} in the droplet has a pronounced effect on corrosion

morphology and hydrogen absorption. The amount of permeated hydrogen through steel increased with increasing Al^{3+} concentrations. Al^{3+} precipitated on the cathodes and promoted HER during the corrosion processes under $AlCl_3$ droplets. The Al-containing precipitated films are suggested to retard iron dissolution before the droplets evaporate.

The work presented in this chapter has been reported in the publications:

Xiaole Han, Masatoshi Sakairi. The promotion effect of aluminium ion on hydrogen entry into steel during atmospheric corrosion. Electrochimica Acta, 458 (2023), 142505.

Xiaole Han, Masatoshi Sakairi. Role of hygroscopic chloride salts on corrosion performance and hydrogen absorption of steel under cyclic wet-dry conditions. Corrosion Science, (2024) 111993.

References

[1] B. Zhang, J. Wang, B. Wu, X.W. Guo, Y.J. Wang, D. Chen, Y.C. Zhang, K. Du, E.E. Oguzie, X.L. Ma, Unmasking chloride attack on the passive film of metals. Nat. Commun. 9(2018) 2559.

[2] M.S. Azevedo, C. Allély, K. Ogle, P. Volovitch, Corrosion mechanisms of Zn (Mg, Al) coated steel in accelerated tests and natural exposure: 1. The role of electrolyte composition in the nature of corrosion products and relative corrosion rate, Corros. Sci. 90 (2015) 472-481.

[3] D. Thierry, D. Persson, G. Luckeneder, K.H. Stellnberger, Atmospheric corrosion of ZnAlMg coated steel during long term atmospheric weathering at different worldwide exposure sites, Corros. Sci. 148 (2019) 338-354.

[4] G. Lazorenko, A. Kasprzhitskii, T. Nazdracheva, Anti-corrosion coatings for protection of steel railway structures exposed to atmospheric environments: a review, Constr. Build. Mater. 288 (2021) 123115.

[5] M. Sakairi, S. Takagi, Effect of surface conditions and relative humidity on hydrogen permeation behavior of zinc coated steels during wet and dry corrosion, ISIJ Int. 56 (2016) 452-458.

[6] K. Sakata, M. Sakairi, J. Kinugasa, Hydrogen Permeation Behavior of Scratch Formed on Zn Coated Steels in Simulated Atmospheric Corrosion Environment, ISIJ Int. 61(2021) 1120-1126.

[7] J. Alcántara, D. de la Fuente, B. Chico, J. Simancas, I. Díaz, M. Morcillo, Marine atmospheric corrosion of carbon steel: A review. Materials 10 (2017) 406.

[8] R. Lindström, J.E. Svensson, L.G. Johansson, The influence of salt deposits on the atmospheric corrosion of zinc. The important role of the sodium ion, J. Electrochem. Soc. 149 (2002) B57.

[9] T. Prosek, D. Thierry, C. Taxén, J. Maixner, Effect of cations on corrosion of zinc and carbon steel covered with chloride deposits under atmospheric conditions, Corros. Sci. 49 (2007) 2676-2693.

[10] C. Liu, V.A. Yang, R.G. Kelly, Inhibition of Cathodic Kinetics by Zn2+ and Mg2+ on AA7050-T7451, J. Electrochem. Soc. 166 (2019) C134.

[11] R.M. Katonaab, R.G. Kelly, C.R. Bryana, R.F. Schallera, A.W. Knight, Use of in situ Raman spectroelectrochemical technique to explore atmospheric corrosion in marine-relevant environments, Electrochem. Commun. 118 (2020) 106768.

[12] S. Zhang, T. Shibata, T. Haruna, Inhibition effect of metal cations to intergranular stress corrosion cracking of sensitized Type 304 stainless steel, Corros. Sci. 47 (2005) 1049-1061.

[13] T. Shibata, Passivity breakdown and stress corrosion cracking of stainless steel, Corros. Sci. 49 (2007) 20-30.

[14] M. Sakairi, R. Sasaki, A. Kaneko, Y. Seki, D. Nagasawa, Evaluation of metal cation effects on galvanic corrosion behavior of the A5052 aluminum alloy in low chloride ion

containing solutions by electrochemical noise impedance, Electrochim. Acta, 131 (2014) 123-129.

[15] K. Otani, M. Sakairi, Effects of metal cations on corrosion of mild steel in model fresh water, Corros. Sci. 111(2016) 302-312.

[16] M.S. Islam, K. Otani, M. Sakairi, Effects of metal cations on mild steel corrosion in 10 mM Cl- aqueous solution, Corros. Sci. 131 (2018) 17-27.

[17] C. Liu, P. Khullar, R.G. Kelly, Acceleration of the cathodic kinetics on aluminum alloys by aluminum ions, J. Electrochem. Soc. 166 (2019) C153.

[18] R.M. Katona, J.C. Carpenter, A.W. Knight, C.R. Bryan, R.F. Schaller, R.G. Kelly, E.J. Schindelholz, Importance of the hydrogen evolution reaction in magnesium chloride solutions on stainless steel, Corros. Sci. 177 (2020) 108935.

[19] C.R. Bryan, A.W. Knight, R.M. Katona, A.C. Sanchez, E.J. Schindelholz, R.F. Schaller, Physical and chemical properties of sea salt deliquescent brines as a function of temperature and relative humidity. Sci. Total Environ. 824 (2022) 154462.

[20] J.R. Galvele, Transport processes and the mechanism of pitting of metals, J. Electrochem. Soc. 123 (1976) 464.

[21] E. Akiyama, S. Li, T. Shinohara, Z. Zhang, K. Tsuzaki, Hydrogen entry into Fe and high strength steels under simulated atmospheric corrosion, Electrochim. Acta 56 (2011) 1799-1805.

[22] S. Ootsuka, S. Fujita, E. Tada, A. Nishikata, T. Tsuru, Evaluation of hydrogen absorption into steel in automobile moving environments, Corros. Sci. 98 (2015) 430-437.

[23] S. Ajito, E. Tada, A. Ooi, A. Nishikata, Hydrogen Absorption Behavior of Pre-Rusted Steels under an NaCl Droplet, J. Electrochem. Soc. 166 (2019) C243.

[24] R.G. Pearson, Hard and soft acids and bases. J. Am. Chem. Soc. 85 (1963) 3533-3539.

[25] S. Zhang, T. Shibata, T. Haruna, Inhibition effect of metal cations to intergranular stress corrosion cracking of sensitized Type 304 stainless steel, Corros. Sci. 47 (2005) 1049-1061.

[26] T. Shibata, Passivity breakdown and stress corrosion cracking of stainless steel, Corros. Sci. 49 (2007) 20-30.

[27] M. Sakairi, R. Sasaki, A. Kaneko, Y. Seki, D. Nagasawa, Evaluation of metal cation effects on galvanic corrosion behavior of the A5052 aluminum alloy in low chloride ion containing solutions by electrochemical noise impedance, Electrochim. Acta, 131 (2014) 123-129.

[28] K. Otani, M. Sakairi, Effects of metal cations on corrosion of mild steel in model fresh water, Corros. Sci. 111(2016) 302-312.

[29] M. Misono, E.I. Ochiai, Y. Saito, Y. Yoneda, A new dual parameter scale for the strength of Lewis acids and bases with the evaluation of their softness, J. inorg. nucl. Chemi. 29 (1967) 2685-2691.

[30] M. Misono, Y. Saito, Evaluation of softness from the stability constants of metal-ion complexes. Bull. Chem. Soc. Jpn, 43 (1970) 3680-3684.

[31] G. Okamoto, Passive film of 18-8 stainless steel structure and its function, Corros. Sci. 13 (1973) 471-489.

[32] U.R. Evans, C.A.J. Taylor, Mechanism of atmospheric rusting, Corros. Sci. 12 (1972) 227-246.

[33] NIST X-ray Photoelectron Spectroscopy Database, NIST Standard Reference Database Number 20, National Institute of Standards and Technology, Gaithersburg MD, 20899 (2000).

[34] N.C. Hosking, M.A. Ström, P.H. Shipway, C.D. Rudd, Corrosion resistance of zinc–magnesium coated steel, Corros. Sci. 49 (2007) 3669-3695.

[35] J. Winiarski, W. Tylus, K. Winiarska, I. Szczygieł, B. Szczygieł, XPS and FT-IR characterization of selected synthetic corrosion products of zinc expected in neutral environment containing chloride ions, J. Spectrosc. (Hindawi), 2018 (2018).

4 Role of Salts in Hydrogen Absorption During Wet-dry Cycles

4.1 Introduction

Atmospheric corrosion is generally regarded as a cyclic wet-dry process attributed to the daily changes in air temperature and relative humidity (RH) over time [1]. With the varying RH and temperature, hygroscopic salts in atmospheric aerosols can introduce conductive electrolytes to the steel surfaces and make the steel products used in atmospheric environments susceptible to corrosion damage [2]. Therefore, the hygroscopic nature of the deposited salts is a primary concern in atmospheric corrosion, and it is essential to elucidate the mechanism of hydrogen entry into steel under salt-induced atmospheric corrosion to reduce the risk of damage to steel structures.

Evans has made vital contributions to the scientific understanding of the atmospheric corrosion mechanism of metals under salt deposits and proposed the importance of hygroscopic salts and corrosion products for the occurrence of electrochemical corrosion. Once RH rises above the deliquescence RH (DRH) of a specific salt, the salt and atmospheric moisture combine to form an electrolyte droplet on the substrate. Conversely, as RH falls below the efflorescence RH (ERH), the droplet evaporates until the salt crystallizes with the release of all remaining water [3]. Consequently, with the variation of RH in the atmospheric environments, the deposited salts are responsible for the thickness of the electrolyte films on steel and determine the duration of the corrosion processes, usually defined as the time of wetness (TOW) [4][5].

In coastal areas, atmospheric aerosols frequently contain significant proportions of hygroscopic salts such as NaCl and $MgCl_2$ [6]. As corrosion proceeds under the salt deposits,

new hygroscopic salts such as $ZnCl_2$ and $AlCl_3$ may emerge due to the anodic dissolution of Zn-Al containing protective coatings on steel [7] [8] [9] [10]. Table 4.1 summarizes the hygroscopic properties of the salts that are supposed to be present in atmospheric corrosion. Schindelholz et al. investigated the relationship between RH and the corrosion response of mild steel contaminated with NaCl and $MgCl_2$ particles and reported that $MgCl_2$ achieved sustained corrosion under a lower RH than NaCl [14] [15]. Based on this finding, Schimo-Aichhorn et al. reported that $MgCl_2$ deposits prolonged the hydrogen insertion into steel more than NaCl during atmospheric corrosion [16]. These results suggest that hygroscopic salts with low DRH values facilitate the introduction of conductive electrolytes to the steel for corrosion to occur and provide a prolonged duration for corrosion to proceed. Given the experimental findings, a reasonable hypothesis is that the concept of TOW is also practicable to understand the association between hygroscopic salts and the hydrogen absorption behaviour in the corrosion processes. Unfortunately, there has been limited literature to provide more experimental evidence for this hypothesis.

Table 3.1. Summary of the preferred values of DRH and ERH of the salts at 25 ˚C

Salt	DRH (%)	ERH (%)	Reference
NaCl	73-77	41-51	[11]
$MgCl_2 \cdot 6H_2O$	30-35	9-11	[11]
$AlCl_3 \cdot 6H_2O$	30[a]	-	[12]
$ZnCl_2$	< 10[a]	-	[13]

[a] The DRH values of $AlCl_3 \cdot 6H_2O$ and $ZnCl_2$ at 25˚C are estimated from the references.

This chapter aims to investigate the role of hygroscopic salts in corrosion and hydrogen entry into steel under cyclic wet-dry conditions and to examine the applicability of the TOW

concept in explaining the role of salts in corrosion and hydrogen absorption activity under salt deposits. As listed in Table 4.1, the distinct difference between the DRH values of the salts is favourable to examining the association between the deliquescence nature of the salts and hydrogen uptake during cyclic wet-dry corrosion.

4.2 Experimental

4.2.1 Sample preparation

The corrosion and hydrogen permeation response of steel after one wet-dry cycle is the concern of this work. The sample was as same as the material used in Chapter 3. The wet-dry corrosion test in Chapter 3 was conducted again to get a corroded sample with salt deposits. The corroded samples were prepared for the following test.

4.2.2 Cyclic corrosion and hydrogen permeation tests

After the first wet-dry cycle, the samples were subjected to a subsequent 11 wet-dry cycles. The experimental procedures are presented in Figure 4.1. The temperature and humidity chamber was used to simulate a cyclic wet-dry environment. After the dyring of the salt droplet, the temperature and humidity inside the chamber were controlled according to a pre-designed procedure. The changes in temperature and humidity in one cycle (6 h) consist of four stages: wet (1 h), drying (1 h), dry (3 h), and wetting (1 h) to the initial wet condition. Each group of corrosion tests was carried out for 11 consecutive cycles (66 h). The cyclic corrosion tests combined with hydrogen detection were carried out at least three times for each salt solution to ascertain the reproducibility of appreciable phenomena during the experiments.

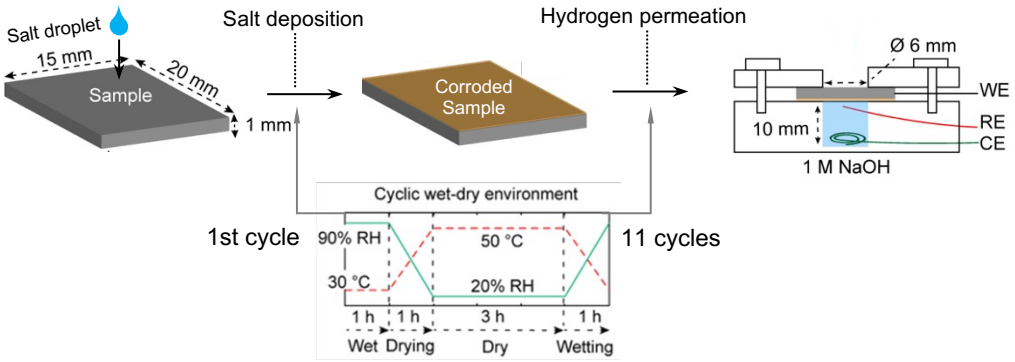

Figure 4.1. Schematic drawing of the experimental procedures.

The hydrogen permeation currents during the cyclic wet-dry corrosion tests were detected using an electrochemical setup consisting of an upper exposed area for corrosion occurrence and a lower electrochemical cell for hydrogen detection was employed to detect the atomic hydrogen that diffused through the samples during cyclic corrosion. The detail of this cell has been introduced in Chapter 2. The changes in the anodic current of the detection cell were recorded during the cyclic corrosion test. In addition, the background current was recorded without performing corrosion upon the sample and subtracted from the detected hydrogen permeation currents to eliminate the interference of temperature on the anodic current fluctuation.

4.2.3 Surface characterisation and analysis

An autofocus USB camera with 1080 p resolution was used for surface imaging during the corrosion process of the sample. The surface changes were captured at intervals of 30 s for the cyclic corrosion test. After the corrosion tests, micrographs of the corroded surface were taken using an optical microscope (OM, MV-550, WRAYMER Inc., Japan). ImageJ was used to

calculate the area statistics of the corroded surfaces of the samples. For characterisation under the rust layer, the corrosion products on the samples were removed carefully using a polishing machine, and then the surfaces were observed using OM.

The surface characterisation and corrosion product analysis were performed with a scanning electron microscope (SEM, JSM-6510-LA, JEOL Ltd., Japan) equipped with an energy dispersive X-ray spectrometer (EDS). The accelerating voltage of the incident electron beam was set at 10 kV for the SEM observation and 20 kV for the ESD analysis. The cross-section of the corroded surface was obtained using a cross-section polisher (IB-19520CCP, JEOL Ltd., Japan) and investigated using SEM and EDS. An auger electron spectrometer (AES, JAMP-9500F, JEOL Ltd., Japan) with a spatial surface resolution of the order of 6 nm was used to characterize the corrosion products. The samples were cut into suitable dimensions using a cut-off machine with water cooling due to the size limitation of the samples for the AES analysis. AES spectra of selected points on the samples were obtained with an accelerating voltage of 10 kV and a probe diameter of the order of 10 nm.

4.3 Results

4.3.1 Corrosion morphology and hydrogen absorption under salt droplets

4.3.1.1 Corrosion and hydrogen absorption under NaCl, $MgCl_2$, and $ZnCl_2$ deposits

In the subsequent 11 wet-dry cycles, as no external supplement of water to the sample surfaces, the hygroscopic nature of the deposited salts was responsible for the formation of electrolytes with the variation of RH and temperature. Figure 4.2 show the corrosion morphology of the samples during the second and third wet-dry cycles. After the droplets

evaporate, the changes in the sample surfaces are not distinct in the following wet-dry cycles. However, some new corrosion products can be observed near the existing rust layers after three cycles, as indicated in the white dotted circles. Additionally, an obvious accumulation of dark corrosion products can be observed on the peripheries of the corroded surface, forming rust rings as indicated in the yellow dotted circles. In the case of the sample under $ZnCl_2$ deposition, the density of dark corrosion products is densely concentrated on one side of the corroded surface, and new corrosion products are also formed on the light corrosion layers. This result indicates the gradual breakdown of the Zn^{2+}-containing films during wet-dry cycles.

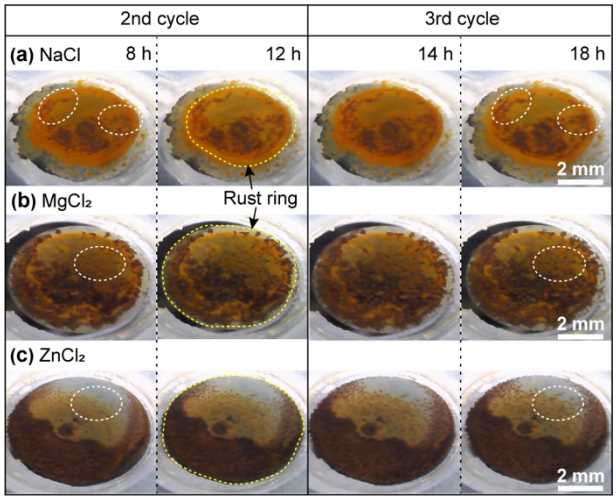

Figure 4.2. Optical images of surface changes in samples under deposited salts of (a) NaCl, (b) $MgCl_2$, and (c) $ZnCl_2$ during the second and third cycles of wet-cry corrosion.

Figure 4.3 (a) shows the changes in hydrogen permeation current densities during the following corrosion processes. Although the current curves exhibit prominent differences in the amplitude of the current density, their variations in each cycle present a similar tendency involving four distinct stages. The permeation currents start from relatively low values in the initial wet period, keeping steady or increasing gradually, then exhibit a conspicuous increase

in the drying period, and finally decrease in the subsequent dry and wetting periods. This variation tendency in each cycle reveals that the hydrogen uptake occurs at a slow rate when the RH is high to maintain the surface being wet, while the drying stage accelerates hydrogen uptake into steel. Regarding the differences in the permeation currents under different exposure conditions, there are three features worth describing. First, the permeation curves under $ZnCl_2$ deposition exhibit larger maximum values than other conditions in most cases, indicating that the hydrogen uptake is promoted by the deposition of $ZnCl_2$. Second, the current under $MgCl_2$ deposition shows a slow decline at the dry stage, suggesting that hydrogen uptake is still active even though the RH is low. The third is that all permeation curves tend to be similar with increasing cycle number and no distinct difference appears in all permeation curves after the tenth cycle.

Figure 4.3 (b) shows the hydrogen contents of the samples under salt deposits in the last eleven cycles. Accompanied by the cyclic corrosion of samples, a considerable amount of permeated hydrogen can be observed in each stage of one wet-dry cycle. The drying and dry stages are the predominant periods for the hydrogen entry into steel. In addition, the hydrogen uptake under $MgCl_2$ and $ZnCl_2$ depositions is more active than that under NaCl deposition. It is worthwhile to note that the electric charge under $ZnCl_2$ deposition has a large deviation during the wet-dry cycle. The large difference in the amount of permeated hydrogen during corrosion under $ZnCl_2$ will be discussed later.

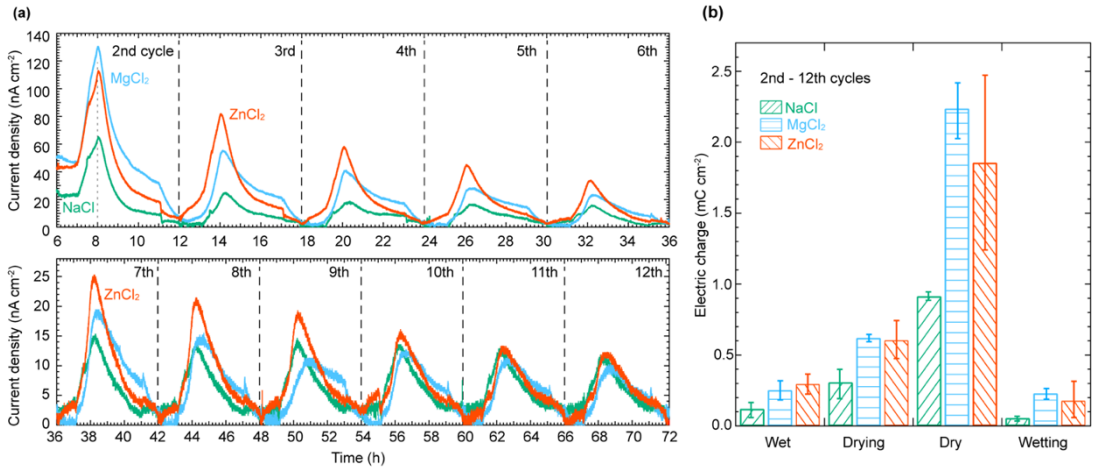

Figure 4.3. (a) Changes in hydrogen permeation current densities of the samples exposed to salt droplets during the last eleven cycles. (b) Electric charges of the samples in the last eleven cycles for each period of a we-dry cycle. Error bars represent standard deviation.

4.3.1.2 Corrosion and hydrogen absorption under $AlCl_3$ deposits with different qualities

In the subsequent cycles (Figure 4.4), the current curves exhibit a similar variation during the wet-dry cycles. The currents begin to increase significantly in the drying period and then decrease after the steel surfaces become dry. The variations in the curves indicate that no appreciable amount of permeated hydrogen exists during the wet period, and the hydrogen entry process mainly happens in the drying period of cyclic corrosion. The increasing temperature and decreasing RH are contributing factors for hydrogen evolution and absorption reactions. As the wet-dry cycle increases, the maximum current values represent a monotonic decrease, and the currents tend to be identical after 11 cycles regardless of the changes in RH and temperature. These phenomena suggest that the hydrogen absorption processes gradually stagnate with the increase of cycle number.

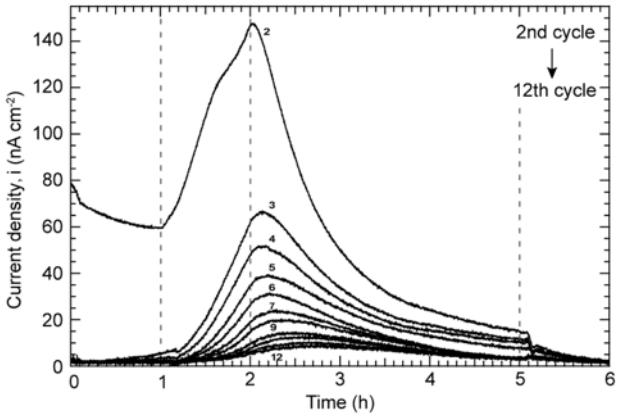

Figure 4.4. Typical change in hydrogen permeation current density of the sample exposed to the droplet of 3.33 mM $AlCl_3$ solution during the subsequent cycles of the cyclic corrosion.

The present study examined the hydrogen permeation behaviour of the samples exposed to four kinds of salt deposits with varying Al^{3+} concentrations. As shown in Figure 4.5, the amount of permeated hydrogen is obtained by integrating the permeation current density with respect to the durations of wet-dry cycles. After eleven wet-dry cycles, the amount of permeated hydrogen through the samples as a function of the concentration of Al^{3+} presents a similar characteristic compared to the first cycle. A particular difference is that the amount of permeated hydrogen at high Al^{3+} concentrations is significantly greater than that at low Al^{3+} concentrations. These results indicate that Al^{3+} still exhibit an acceleration effect on hydrogen entry into steel during the corrosion process under the rust layers.

As for the corrosion morphology shown in Figure 4.6, in the subsequent second and third cycles, there is a perceptible increase in the amounts of brown corrosion products on the sample surfaces. Since no extra water was supplied to the exposed surfaces during the cyclic corrosion tests, the deposited salt particles in the rust layers are supposed to absorb moisture and facilitate corrosion and hydrogen entry into samples. As the number of corrosion cycles increases, the

increased thickness of the rust layers makes it difficult for the electrolytes produced from the salts to reach the steel surface through the thick rust layers. The decrease in the thickness of electrolytes on the steel inhibits the corrosion processes, resulting in a decrease in the amount of permeated hydrogen.

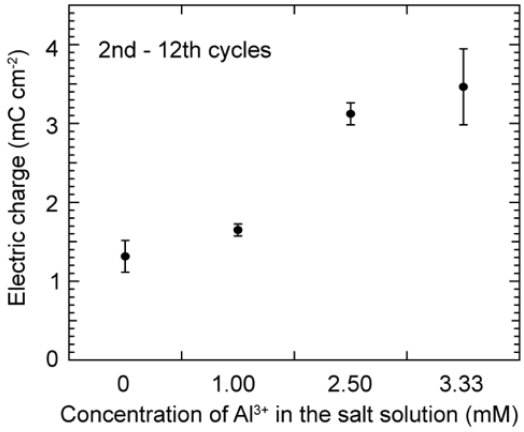

Figure 4.5. Comparison of electric charges of the samples as a function of the concentration of Al^{3+} in the salt solutions. Error bars represent one standard deviation.

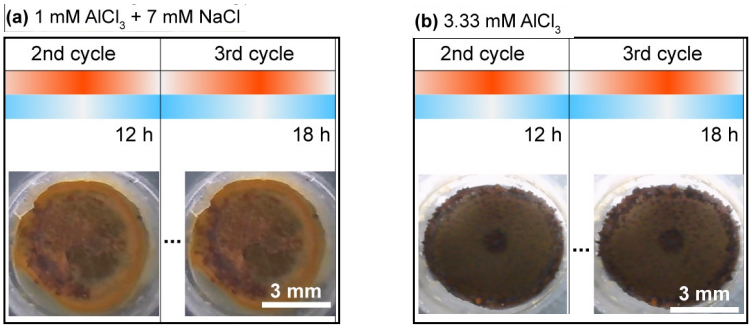

Figure 4.6. Optical images of corrosion morphology of the samples under (a) 1 mM $AlCl_3$ + 7 mM NaCl and (b) 3.33 mM $AlCl_3$ after the 2nd and 3rd corrosion cycle.

In addition to the rust layers, the deliquescent ability of the deposited salts is also responsible for the thickness of the electrolyte layer. As $AlCl_3$ can absorb water and deliquesce more easily than NaCl, the increase in the amount of permeated hydrogen with increasing concentration of Al^{3+} is attributed to the increase in the amount of the deposited $AlCl_3$, which

increases the volume of the electrolytes and provides an extended duration for corrosion and hydrogen entry into steel.

4.3.2 Characterization of corroded surfaces using SEM-EDS and AES

4.3.2.1 Characterization of samples under NaCl, $MgCl_2$, and $ZnCl_2$ deposits

To investigate the effect of salts on the corrosion morphology of samples after 11 wet-dry cycles, SEM observation and EDS analysis were performed on the corroded surfaces. Figure 4.7 shows a corroded area near the rust ring of the sample under NaCl. Some raised spherical corrosion products can be observed adjacent to the rust ring, while the relatively uniform ones are homogeneously distributed in the flat region near the central area of the exposed surface. The EDS elemental mapping shows that Cl is particularly abundant in the raised structures of the corrosion products, and the detection of Na and Cl in the same area (Figure 4.7 (a), white arrows) indicates the accumulation of NaCl around the rust ring after 12 cycles of corrosion. In Figure 4.7 (b), the SEM observations on the sample exposed to $MgCl_2$ show that the surface is covered by raised corrosion products and a portion of the surface is not significantly corroded, as indicated in the white arrow. Moreover, the EDS analysis illustrates the presence of a great proportion of Mg-containing precipitation layers adjacent to the raised corrosion products.

The corrosion products formed on the sample exposed to $ZnCl_2$ exhibit a distinct boundary between the flat (Area 1) and raised (Area 2) regions. EDS analysis performed on a selected boundary area shows that the raised area contains large amounts of corrosion products and Cl is significantly abundant in the raised spherical corrosion products similar to the other two salts. In particular, Zn exhibits no particular aggregation on the corroded surface and only a rare proportion is detected on the flat area. To further determine the presence of Zn on the surface,

AES analysis was carried out on the flat region (Figure 4.8 (a), Area 1) and raised region (Figure 4.8 (a), Area 2) and the results are presented in Figure 4.8 (b). The Zn is primarily found in the uniform rust layer but not in the raised corrosion products. The detailed auger spectra of Zn (Figure 4.8 (c)) illustrate that Zn is probably in the form of its oxide and hydroxide as the kinetic energy of Zn peaks shows a slight shift in the energy reduction direction compared with the standard spectrum.

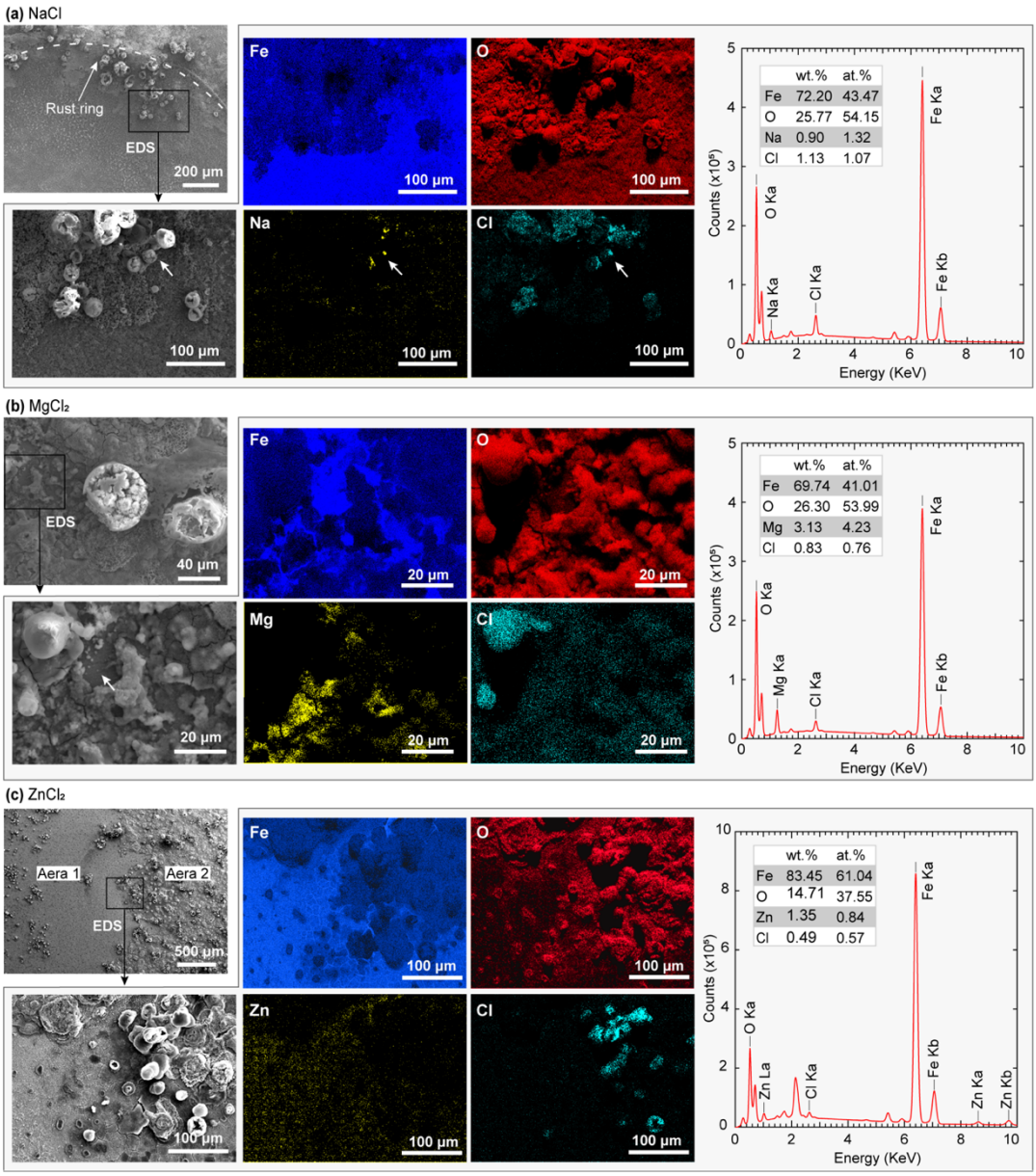

Figure 4.7. SEM and EDS elemental mapping images of the samples after corrosion under

salt droplets of (a) 10 mM NaCl, (b) 5 mM $MgCl_2$, and (c) 5 mM $ZnCl_2$ for twelve cycles.

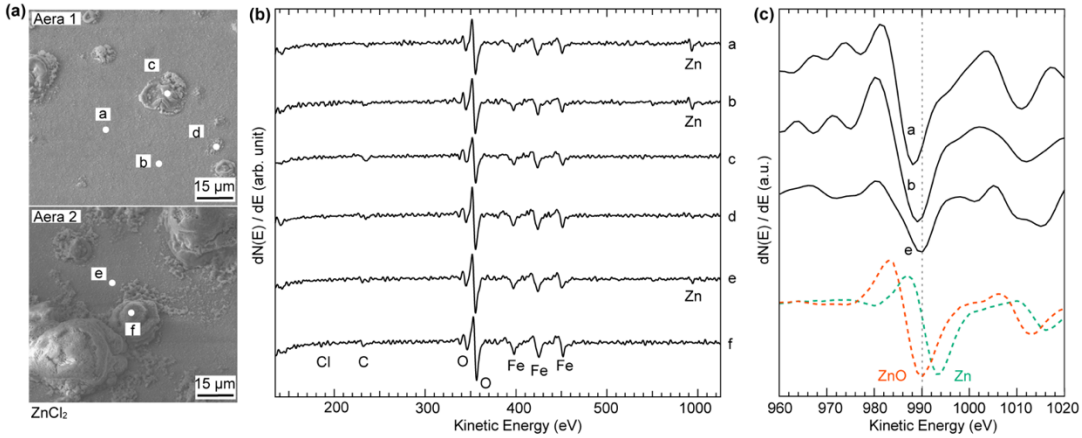

Figure 4.8. (a) SEM images of two areas marked in Fig. 7 (c) of the corroded sample under $ZnCl_2$. (b) AES spectra of the selected points in (a). (c) Comparison of the detected AES spectra in the Zn spectral range with the standard spectra.

4.3.2.1 Characterization of samples under $AlCl_3$ deposits

The SEM observation and EDS analysis were performed on the sample corroded under the $AlCl_3$ droplet and the results are presented in Figure 4.9. The corroded surface is composed of hump-shaped products and relatively flat layers. The EDS mapping demonstrates the presence of Al and Cl elements on the corroded surface. Of note, Cl elements are particularly abundant in the hump-shaped corrosion products, while Al elements are enriched in some circular spots on the flat layers, as indicated by yellow arrows in Figure 4.9 (b). Figure 4.9 (c) presents the characteristic of the Al-rich structure, which is a raised spot surrounded by a ring of corrosion products. These results imply that the Al and Cl elements are distributed separately during the corrosion processes. Al-rich area is supposed to be the cathodic site, while the Cl-rich area is the anodic site.

To further investigate the thin rust layers, AES analysis was carried out on the flat region

of the corroded surface. Note that the sample was washed with ultrapure water before the analysis. Figure 4.10 (a) shows an area of the flat region, which is composed of a uniform rust layer and some raised corrosion products. As shown in the AES spectra (Figure 4.10 (b)), Al elements are detected in the uniform rust layer but not in the raised structures. In addition, a comparison of the auger spectra of Al with the Al_2O_3 peak of the standard spectra demonstrates that Al exists in the form of Al oxide (Figure 4.10 (c)). These results validate the precipitation of Al compounds during cyclic corrosion.

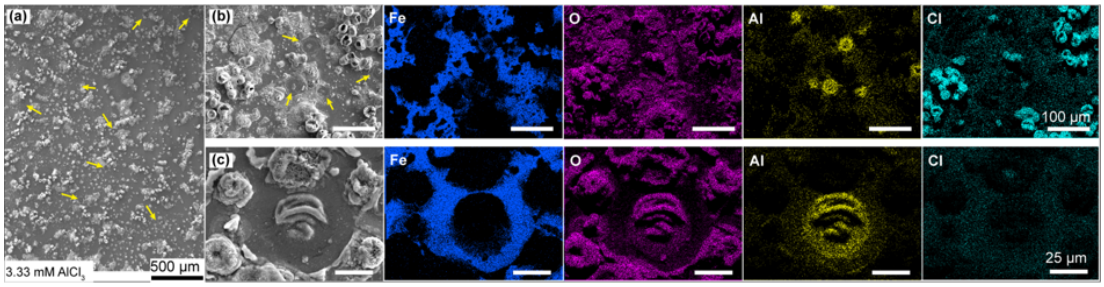

Figure 4.9. SEM-EDS images of the sample under $AlCl_3$ droplet after 12 wet-dry cycles. (a) SEM image of the corrosion products on the sample. (b) SEM image of an expanded area in (a) and the corresponding EDS mapping images of Fe, O, Al, and Cl. (c) SEM-EDS images of an Al-rich area in (a). Yellow arrows indicate the Al-rich areas.

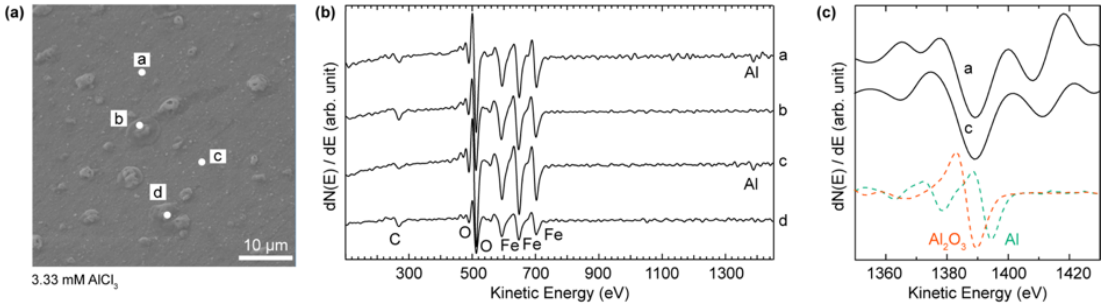

Figure 4.10. (a) A detailed SEM image of a flat area of the corroded surface in Fig. 8(a). (b) AES spectra of the selected points in (a). (c) Comparison of the detected AES spectra in the Al spectral range with the standard spectra.

4.3.3 Analysis of corroded surfaces under rust layers

4.3.3.1 Section analysis of samples under $AlCl_3$ deposits

In addition to the corrosion process and hydrogen absorption under the initial salt droplets, hydrogen entry that occurs after the droplets evaporate and the rust layers cover the steel surfaces is also noticeable in cyclic corrosion. To determine the influence of Al^{3+} on the corrosion activity under the rust layers, the corrosion products were carefully removed from the samples that were corroded for 12 cycles. Figure 4.11 shows the optical images of the corroded samples and the images after removing the corrosion products. The corrosion products of the samples under different deposited salts present different characteristics. In the case of the sample corroded under a mixed salt solution with a high Na^+ concentration, a large proportion of corrosion products are yellow and relatively flat, and the raised brown ones prefer to form towards one side of the exposed surface, attributed to the airflow inside the chamber. Regarding the sample corroded under the $AlCl_3$ droplet, the exposed surface shows a distinctive rust spot near the central region (Figure 4.11 (b), white arrow) and a ring-shaped rust layer along the peripheral region (Figure 4.11 (b), yellow arrow). The brown corrosion products in hump shapes occupy a greater portion of the exposed surface.

After removing the rust layers for both samples, the hollow-shaped regions are prominently distributed under the brown corrosion products, leaving the near-intact steel substrate under the relatively flat rust layers. The hollow-shaped regions are supposed to act as the anodic sites during cyclic corrosion, and the proportion of such regions on the sample under $AlCl_3$ is greater than mixed salts. It is generally recognized that the corrosion processes proceed under electrolyte layers according to the iron dissolution in the anodic site and ORR in the

cathodic site. With the anodic iron dissolution, a proportion of iron ions is supposed to hydrolyze and induce localized acidification in the anodic sites:

$$4Fe^{2+} + O_2 + 6H_2O \rightarrow 4FeOOH + 8H^+ \quad (4.1)$$

$$Fe^{3+} + 3H_2O \rightarrow Fe(OH)_3 + 3H^+ \quad (4.2)$$

which is considered prominent sources for hydrogen evolution and absorption during cyclic corrosion. These findings indicate that $AlCl_3$ demonstrate a contributing role in localized corrosion and acidification during the cyclic corrosion process, which facilitates hydrogen entry into steel.

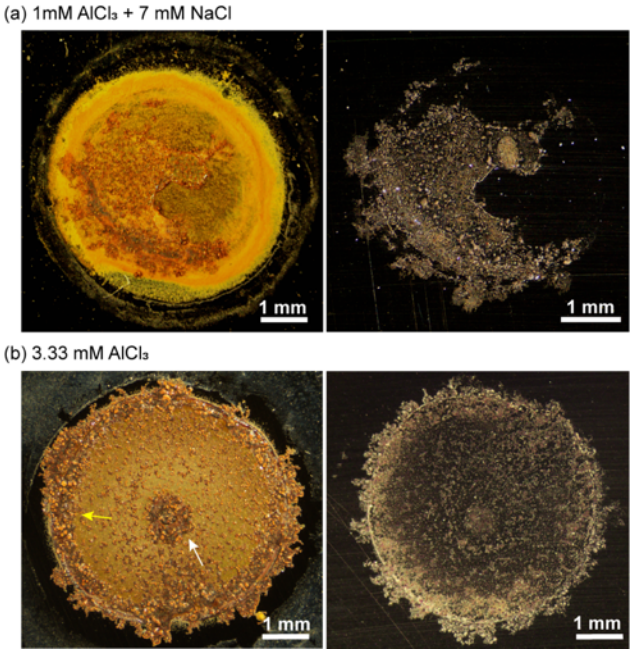

Figure 4.11. Optical images of the corroded and rust-removed samples under (a) 1 mM $AlCl_3$ + 7 mM NaCl and (b) 3.33 mM $AlCl_3$ after 12 wet-dry cycles.

Combining the results of surface observation and hydrogen permeation, although an apparent dissolution of iron appears in the central area under the droplet due to the difference in oxygen concentration, the hydrolysis of metal cations is not expected to produce a local acid

environment as the pH buffering effect of the droplet. As water evaporates, the increase in the concentration of Cl^- will result in a local breakdown of the precipitated film and induce the anodic dissolution of iron underneath the brown corrosion products. In this case, the localized corrosion and hydrolysis reactions of metal cations are expected to facilitate the generation of absorbed hydrogen.

To corroborate the finding that $AlCl_3$ facilitate localized corrosion, the cross-sectional samples of the corroded surface under 3.33 mM $AlCl_3$ were prepared. The rust spot in the central area and the ring-shaped rust layer on the edge side of the corroded surface were selected as cutting positions for analysis. As shown in Figure 4.12 (a), a pronounced corrosion pit develops underneath the rust layers in the central area, showing a cavity structure with porous corrosion products. Apart from the serious central pit, the corroded surface in the central area is mainly composed of porous pits and thin rust layers. These porous structures are expected to provide significant venues for the deposited salts to deliquesce and initiate corrosion underneath the rust layers.

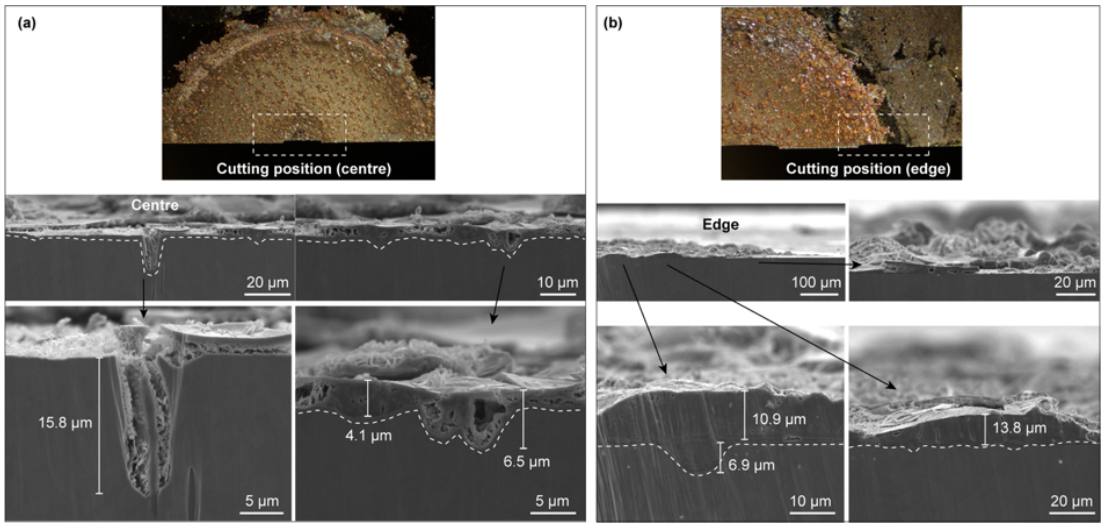

Figure 4.12. Cross-sectional images of (a) the centre and (b) the edge of the rust layers formed on the samples under $AlCl_3$ droplets after 12 wet-dry cycles.

On the other hand, the edge side of the corroded surface is suggested as the cathodic site during the droplet corrosion process, where corrosion products prefer to accumulate. The thickness of the rust layers is significantly greater than that near the central area of the corroded surface, as shown in Figure 4.12 (b). In addition, the rust layers show a compact structure rather than a porous one formed in the central area. Notably, a corrosion pit filled with corrosion products can be found under the rust layer, indicating that the edge side of the exposed surface is expected to develop new anodic sites during cyclic corrosion. It is notable that the pit depth under the thick rust layers on the edge side is less than that near the central area. As the presence of electrolytes introduced by the deposited salts is essential for corrosion to proceed and the thick rust is expected to obstruct the diffusion of moisture, the activity of the anodic dissolution of steel under the thick rust layers is suggested to be sluggish.

Together, the anodic dissolution begins due to the initial geometric shape of the droplets and proceeds under the rust layers. After the droplet evaporates, the localized dissolution of iron and hydrolysis reactions of metal cations produce an acidic environment under the rust layers, facilitating hydrogen entry into steel. As the wet-dry cycle proceeds, the processes of iron dissolution and the combined hydrolysis reactions of metal cations will be gradually retarded due to the increasing thickness of the rust layers.

4.3.3.2 Section analysis of samples under NaCl, $MgCl_2$, and $ZnCl_2$ deposits

The cross-sectional images of the corroded surfaces provide additional information on the morphology of the corrosion products. The rust layers formed on the sample under NaCl are porous and contain cracks, as shown in Figure 4.13 (a). Abundant porous structures can be

observed in the inner rust layer near the steel substrate. Furthermore, the interface between the rust layer and the steel substrate is relatively flat compared with other salts, as indicated by the dashed lines. In the case of the sample under $MgCl_2$ (Figure 4.13 (b)), the thickness of the rust layers is significantly greater than the sample under NaCl. In addition, deep and elliptical corrosion pits are formed under hill-shaped corrosion products. Similarly, the rust layer under $MgCl_2$ also contained cracks but in near horizontal shapes, and the porous structures are remarkably abundant in the hill-shaped layers.

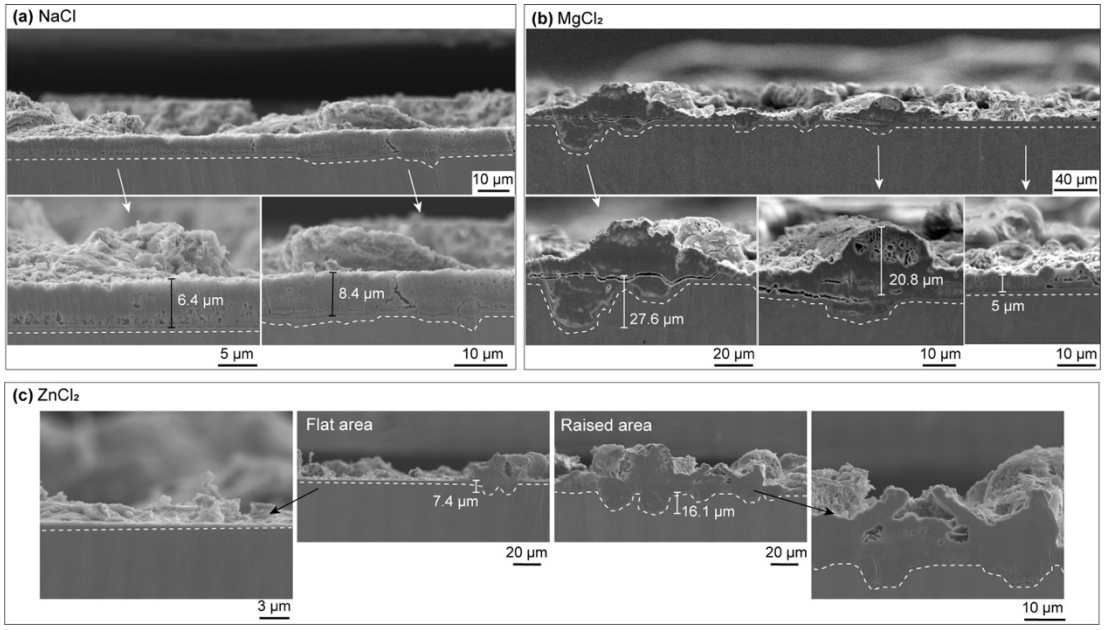

Figure 4.13. Cross-sectional images of the rust layers formed on the samples after cyclic corrosion under (a) 10 mM NaCl, (b) 5 mM $MgCl_2$, and (c) 5 mM $ZnCl_2$.

As for the sample under $ZnCl_2$, Figure 4.13 (c) shows two distinct areas under flat and raised corrosion products, corresponding to Area 1 and Area 2 in Figure 4.7 (c), respectively. The flat area, where Zn has been determined to be present, has a relatively thin rust layer and suffers from a slight pitting corrosion. The area under a large amount of raised corrosion

products presents a similar feature to that under $MgCl_2$, consisting of pits and porous rust layers.

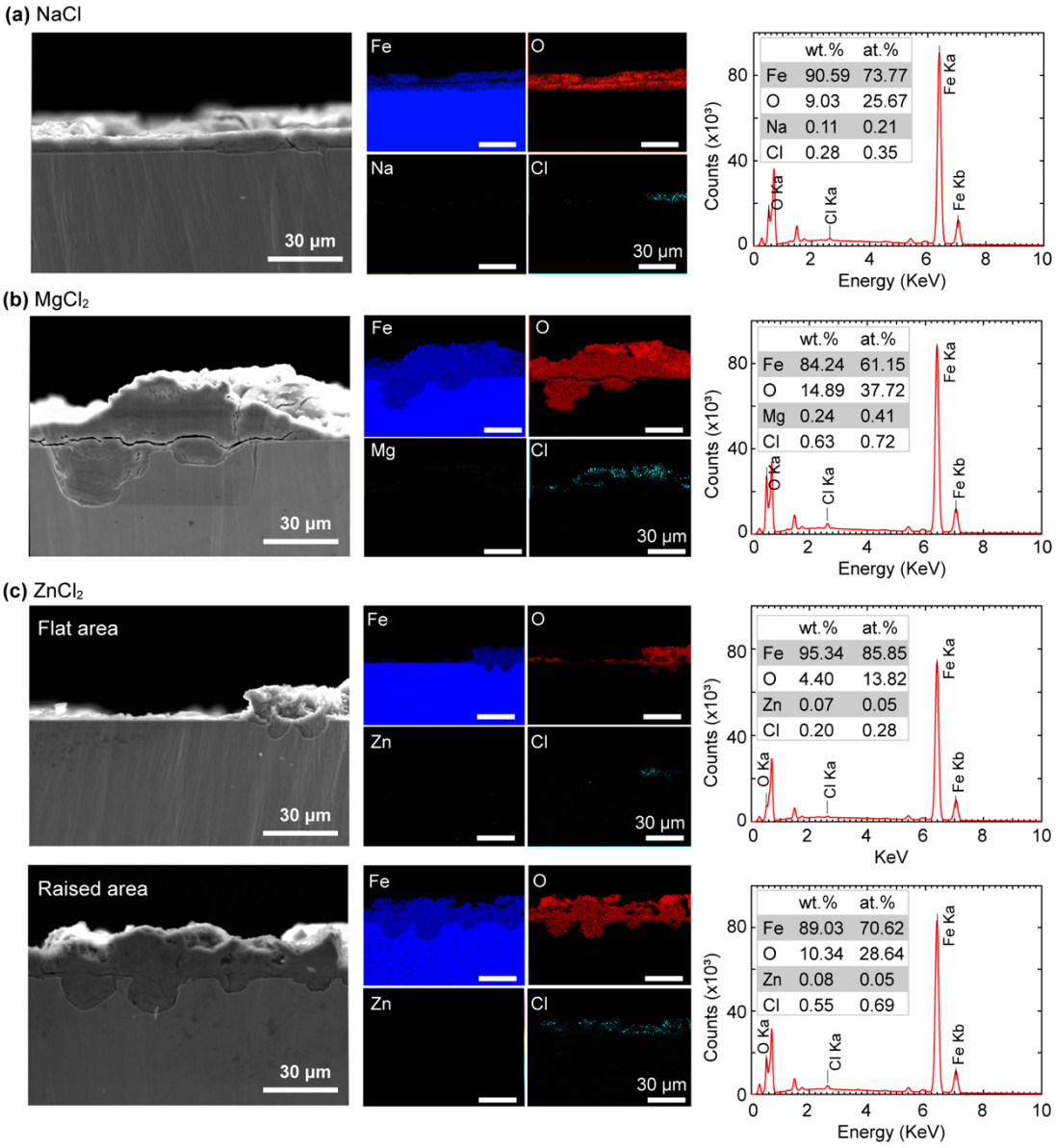

Figure 4.14. EDS elemental mapping images of the cross-sectional samples after corrosion under salt droplets of (a) 10 mM NaCl, (b) 5 mM $MgCl_2$, and (c) 5 mM $ZnCl_2$ for 11 cycles.

Although it is rare to find the elements of Na, Mg, and Zn in the rust layers from the EDS elemental mapping on the cross-sectional samples (Figure 4.14), the element Cl is particularly abundant near the surface of the hill-shaped corrosion products. The distinct boundary between

the rust layer and steel substrate also indicates the presence of larger pits under $MgCl_2$ and $ZnCl_2$ deposits than NaCl. As mentioned previously, lower ERH and DRH values of the $MgCl_2$ and $ZnCl_2$ deposits can provide a prolonged period for corrosion proceeding and hydrogen entry into steel. Coupled with the results of cross-sectional images, the greater number of pits under $MgCl_2$ and $ZnCl_2$ deposits than NaCl is probably attributed to the higher deliquescent properties of the salts. Accordingly, it is reasonable to assume that the promotion effect of hygroscopic salts on the pitting development under rust layers may be responsible for the higher hydrogen permeation charge during wet-dry corrosion.

4.3.4 Area calculation of corroded surfaces under rust layers

To corroborate the finding of the acceleration effect of pitting corrosion on the hydrogen entry into steel, this study attempted to calculate the pitting area of the corroded samples under different salt depositions. As shown in Figure 4.15, each sample after corrosion under different deposited salts has distinctive characteristics of corrosion products.

The corroded surfaces of each sample mainly consist of a ring-shaped brown layer along the peripheral region and other orange corrosion products. Significantly, the brown ones correspond to the hill-shaped rust layers where appreciable pits can be found, as shown in Figure 4.13. The orange ones, by contrast, are related to the flat rust layers where general corrosion predominately occurs. From the images after removing the rust layer using the polishing machine, the pitted areas are prominently distributed under the brown hill-shaped corrosion products, leaving the relatively uncorroded steel substrate under the orange ones. This finding corroborates the connection between the pitting region and the brown rust area. The

area beneath the brown rust ring is one of the prime places for pitting corrosion. In particular, the sample under $ZnCl_2$ shows a serious pitted region under a brown spot near the central area (Figure 4.15, red arrow), corresponding to the previous black spot that appeared in the wet period of the first cycle). This result confirms the corrosion mechanism that initial anodic dissolution usually happens near the central area of the salt droplets.

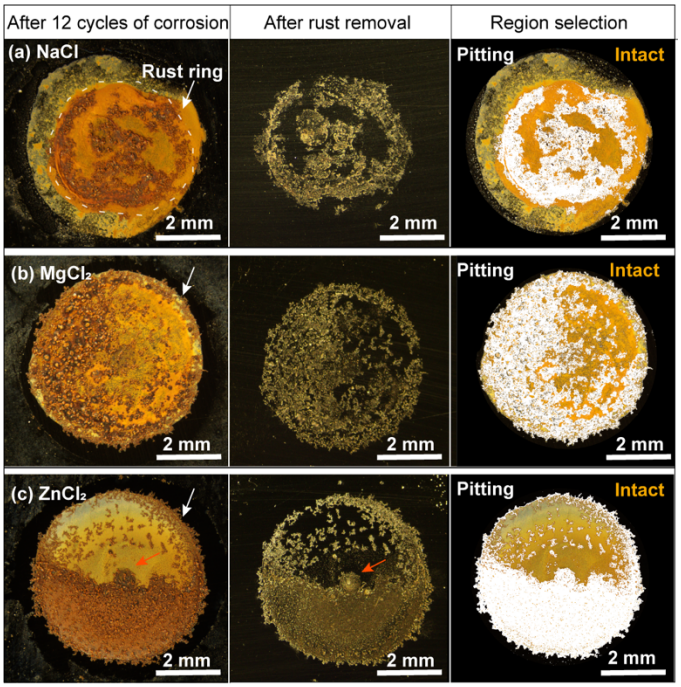

Figure 4.15. Optical images and region selection for the samples after cyclic corrosion under (a) 10 mM NaCl, (b) 5 mM $MgCl_2$, and (c) 5 mM $ZnCl_2$.

For the sake of simplicity, the brown and orange corrosion products were categorised as pitting and intact regions, respectively. Based on the colour difference in the corroded products, region selection was carried out in ImageJ software. Since the brown colour represents the pitting area, the red-green-blue (RGB) codes from (0, 0, 0) to (255, 120-140, 255) were derived from the optical images (Figure 4.15). The ratio of the pitting area to the entire exposed area was calculated and plotted against the amount of diffused hydrogen under five kinds of salt

depositions. As shown in Figure 4.16, the greater amount of permeated hydrogen is related to the greater percentage of the pitting area. The large difference in the pitting area under the same composition of salt droplets results in a large deviation in the amount of permeated hydrogen. Moreover, the results show that the amount of permeated hydrogen of the samples under $MgCl_2$-containing salts is greater than that under $ZnCl_2$, although the samples have a similar percentage of pitting area. Based on the cross-sectional images of the pitting area under $MgCl_2$ and $ZnCl_2$, the deeper pits under $MgCl_2$ are supposed to be responsible for the more active entry of hydrogen into the steel.

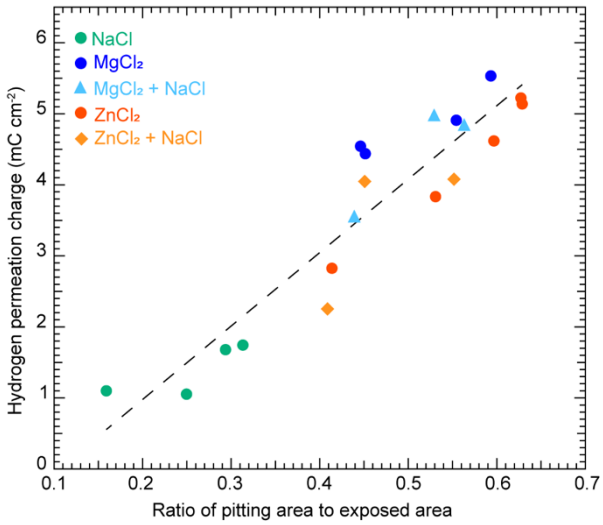

Figure 4.16. Hydrogen permeation charges of the samples after cyclic corrosion under five kinds of salt droplets as a function of the ratio of pitting area to exposed area.

4.4 Discussion

4.4.1 Role of salts in corrosion and hydrogen absorption after droplet drying

As water evaporates in the drying stage, the increasing concentration of aggressive anions leads to the breakdown of passive films and results in accelerated corrosion of steel and

hydrogen absorption process. It is known that the presence of electrolytes is essential for electrochemical corrosion to proceed, and therefore the deliquescence properties of the salts will play a predominant role after droplet drying. The lower DRH and ERH values of the salts represent the stronger capacity to absorb moisture, providing a longer time for the existence of a thin layer of electrolyte. Further, it is important to consider the high concentration of aggressive anions such as Cl^- in the thin electrolyte layer. Hydrogen entry into steel can be accelerated in the presence of a thin electrolyte layer with a high concentration of corrosive ions. Therefore, high hygroscopic salts such as $MgCl_2$ and $ZnCl_2$ afford a prolonged TOW for corrosion and hydrogen absorption reactions to proceed during wet-dry cycles.

On the other hand, the presence of rust layers is another important factor influencing the hygroscopicity of the deposited salts on steel surfaces. As the rust layers contain narrow cracks and porous structures. Attributing to the capillary condensation of the porous structure, the deposited hygroscopic salts can retain the presence of electrolytes within the porous rust layers under low RH conditions, extending the TOW for corrosion during wet-dry cycles, as illustrated in Figure 4.17 (a). Furthermore, the remaining electrolytes within the rust layers are supposed to have a high concentration of corrosive ions. This is probably the reason why corrosion and hydrogen entry can take place under $MgCl_2$ deposits even when the corroded surfaces have a dry appearance in the dry stage. Although $ZnCl_2$ deposits have lower DRH and ERH values than $MgCl_2$, the presence of ZnO inhibits the formation of porous rust layers, resulting in a lower quantity of absorbed hydrogen after an entire wet-dry cycle. After the breakdown of the protective films due to the increasing concentration of corrosive ions in the drying period (Figure 4.17 (d)), porous corrosion products accumulate around the anodic dissolution sites,

facilitating the absorption of moisture and accelerating corrosion and hydrogen entry under the rust layers. Overall, both the hygroscopicity of the salts and the porous structure of the rust layers are crucial factors in determining the TOW for corrosion and hydrogen absorption processes during wet-dry cycles.

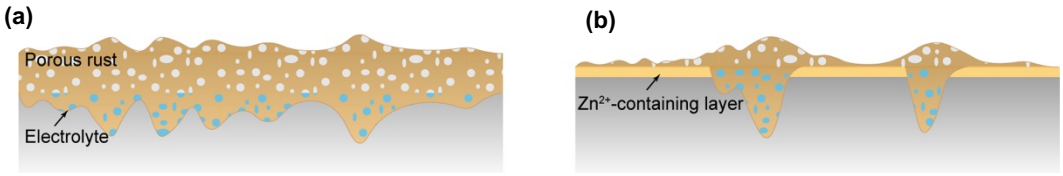

Figure 4.17. Proposed models of (a) the porous rust layer contributing to the formation of thin electrolyte layer at low humidity and (b) the breakdown of Zn^{2+}-containing layer due to the increasing concentration of chloride ion as water evaporates.

Regarding the mechanism of hydrogen absorption after droplet drying and rust formation, pitting corrosion and localized acidification under rust layers are suggested to play a vital role in the wet-dry cycles. After the droplets evaporate, the remaining electrolytes with a high concentration of chloride inside the thick and porous rust layers are favourable for the development of new pits under the rust layers, contributing to decreasing pH inside the pits. Since the rust layers retard the migration of ions between the anodic and cathodic areas, the hydrolysis of the dissolved iron also results in acidification inside the pits. The hydrogen adsorption reaction takes place according to the Volmer mechanism, i.e., the electrochemical reduction of proton in acid solutions (Eq. 4.3):

$$H^+ + e^- \rightarrow H_{ad} \quad (4.3)$$

The adsorbed hydrogen atoms are subsequently absorbed by the steel substrate (Eq. 4.4):

$$H_{ad} \rightarrow H_{ab} \quad (4.4)$$

Attributing the decreasing pH inside the pits, the driving force for hydrogen evolution reaction is promoted when corrosion potential is assumed to be constant. As a result, the adsorption and absorption reactions of hydrogen are accelerated under the rust layers.

Together, the hygroscopic salts and porous rust layers introduce thin electrolyte layers with high chloride concentrations to the steel surface and contribute to localized acidification under the rust layers. When the deposited salts, such as $MgCl_2$ and $ZnCl_2$, have a higher ability to absorb moisture, the TOW is prolonged for corrosion and hydrogen entry into steel. However, with the increasing we-dry cycle number, the increasing thickness of stable rust layers is supposed to retard the access of electrolytes and oxygen to the steel surface; therefore, the corrosion and hydrogen absorption processes will decline progressively under cyclic wet-dry conditions.

4.5 Conclusions

In this chapter, corroded steel with an initial deposition of salt deposits was used to examine the corrosion morphology and the associated hydrogen permeation behaviour of steel after several wet-dry cycles. Several conclusions can be drawn as follows:

- After water evaporates and steel surfaces become apparently dry, the hygroscopic property of the salts deposited within the porous rust layers plays a dominant role in the corrosion and hydrogen absorption processes. The salts with low deliquescence values retain the presence of thin electrolyte layers with high chloride concentrations within the porous rust structures, affording a prolonged TOW for localized corrosion.
- Pitting corrosion and localized acidification under rust layers are responsible for

accelerated hydrogen entry into steel. The presence of ZnO film retards the development of pitting corrosion, thereby reducing the amount of absorbed hydrogen during an entire wet-dry cycle.

The work presented in this chapter has been reported in the publications:

Xiaole Han, Masatoshi Sakairi. The promotion effect of aluminium ion on hydrogen entry into steel during atmospheric corrosion. Electrochimica Acta, 458 (2023), 142505.

Xiaole Han, Masatoshi Sakairi. Role of hygroscopic chloride salts on corrosion performance and hydrogen absorption of steel under cyclic wet-dry conditions. Corrosion Science, (2024) 111993.

References

[1] P.R. Roberge, Atmospheric Corrosion, in: R.W. Revie (Ed.), Uhlig's Corrosion Handbook, third ed., Wiley, New York, 2011, pp. 299-326.

[2] C.R. Bryan, A.W. Knight, R.M. Katona, A.C. Sanchez, E.J. Schindelholz, R.F. Schaller, Physical and chemical properties of sea salt deliquescent brines as a function of temperature and relative humidity. Sci. Total Environ. 824 (2022) 154462.

[3] S.T. Martin, Phase transitions of aqueous atmospheric particles. Chem Rev. 100 (2000) 3403-3454.

[4] I.S. Cole, W.D. Ganther, J.D. Sinclair, D. Lau, D.A. Paterson, A study of the wetting of metal surfaces in order to understand the processes controlling atmospheric corrosion, J. Electrochem. Soc. 151 (2004) B627.

[5] E. Schindelholz, R.G. Kelly, Wetting phenomena and time of wetness in atmospheric corrosion: a review, Corr. Rev. 30 (2012) 135-170.

[6] C.R. Bryan, A.W. Knight, R.M. Katona, A.C. Sanchez, E.J. Schindelholz, R.F. Schaller, Physical and chemical properties of sea salt deliquescent brines as a function of

temperature and relative humidity. Sci. Total Environ. 824 (2022) 154462.

[7] M.S. Azevedo, C. Allély, K. Ogle, P. Volovitch, Corrosion mechanisms of Zn (Mg, Al) coated steel in accelerated tests and natural exposure: 1. The role of electrolyte composition in the nature of corrosion products and relative corrosion rate, Corros. Sci. 90 (2015) 472-481.

[8] D. Thierry, D. Persson, G. Luckeneder, K.H. Stellnberger, Atmospheric corrosion of ZnAlMg coated steel during long term atmospheric weathering at different worldwide exposure sites, Corros. Sci. 148 (2019) 338-354.

[9] M. Sakairi, S. Takagi, Effect of surface conditions and relative humidity on hydrogen permeation behavior of zinc coated steels during wet and dry corrosion, ISIJ Int. 56 (2016) 452-458.

[10] K. Sakata, M. Sakairi, J. Kinugasa, Hydrogen Permeation Behavior of Scratch Formed on Zn Coated Steels in Simulated Atmospheric Corrosion Environment, ISIJ Int. 61(2021) 1120-1126.

[11] C. Peng, L. Chen, M. Tang, A database for deliquescence and efflorescence relative humidities of compounds with atmospheric relevance, Fundament. Res. 2 (2022) 578-587.

[12] D.B. Blücher, J.E. Svensson, L.G. Johansson, The influence of CO2, AlCl3·6H2O, MgCl2·6H2O, Na2SO4 and NaCl on the atmospheric corrosion of aluminum. Corros. Sci. 48 (2006) 1848-1866.

[13] T. Herzog, W. Müller, W. Spiegel, J. Brell, D. Molitor, D. Schneider, Corrosion caused by dew point and deliquescent salts in the boiler and flue gas cleaning, K.J. Thomé-Kozmiensky, S. Thiel (Eds.), Waste Management, 3, Recycling and Recovery, TK Verlag, Neuruppin (2012), pp. 343-358.

[14] E. Schindelholz, B.E. Risteen, R.G. Kelly, Effect of relative humidity on corrosion of steel under sea salt aerosol proxies: I. NaCl, J. Electrochem. Soc. 161 (2014) C450-C459.

[15] E. Schindelholz, B.E. Risteen, R.G. Kelly, Effect of relative humidity on corrosion of steel under sea salt aerosol proxies: II. MgCl2, artificial seawater, J. Electrochem. Soc.

161 (2014) C460-C470.

[16] G. Schimo-Aichhorn, I. Traxler, A. Muhr, C. Commenda, D. Rudomilova, O. Schneeweiss, G. Luckeneder, H. Duchaczek, K.H. Stellnberger, J. Faderl, T. Prošek, Hydrogen Insertion into Complex-Phase High-Strength Steel during Atmospheric Corrosion at Low Relative Humidity, Metals 12 (2022) 624.

5 Summary

The overall objective of this thesis was to investigate how environmental factors and salt depositions affect hydrogen absorption into steel during atmospheric corrosion. The key findings with respect to this aim are summarized as follows.

(1) Environmental impact of RH on hydrogen absorption into steel. The effect of RH on the corrosion and hydrogen absorption of steel under NaCl deposit was investigated by controlling the RH at different levels below the DRH of NaCl during wet-dry cycles. The results suggest that the hydrogen absorption into steel can occur even if the surrounding RH is below the DRH of NaCl. The amount of permeated hydrogen increases with higher RH of the dry stage during the wet-dry cycles, which is attributed to the prolonged period of the presence of liquid phase inside the corrosion products.

(2) The effect of metal cations on corrosion performance under salt droplets. After understanding the importance of DRH of salt in atmospheric corrosion, an analysis of corrosion and hydrogen permeation of steel under aqueous NaCl, $MgCl_2$, $ZnCl_2$, and $AlCl_3$ solution droplets was conducted to investigate the role of different hygroscopic slats and their metal cations in the cyclic wet-dry corrosion. When corrosion occurs under salt droplets containing Mg^{2+}, Zn^{2+}, and Al^{3+}, cation-containing layers are supposed to form on the steel surfaces and present corrosion resistance. Based on the HSAB concept, the metal cations with higher cation hardness are easier to combine with the hard bases such as H_2O and OH^- of the passive films, forming stable protective passive films against corrosion attack under salt droplets.

(3) The effect of salt depositions on hydrogen entry into steels during wet-dry cycles. After water evaporates and steel surfaces become apparently dry, the hygroscopic property of the salts deposited within the porous rust layers plays a dominant role in the corrosion and hydrogen absorption processes. The salts with low deliquescence values retain the presence of thin electrolyte layers with high chloride concentrations within the porous rust structures, affording a prolonged TOW for corrosion. Based on the experimental results and analysis, the TOW and HSAB concepts are applicable in explaining the role of salts in the corrosion and hydrogen absorption activity of high-strength low alloy steel during simulated atmospheric corrosion. This study suggests that localised pitting and acidification under rust layers are responsible for accelerated hydrogen entry into steel during wet-dry cycles.

List of Research Accomplishments

Journal publications:

(Thesis related papers)

[1] Xiaole Han and Masatoshi Sakairi. Hydrogen permeation behavior of steel under wet/dry corrosion with changes in relative humidity at the dry period, *ISIJ International*, 61 (2021) 1194-1200.

[2] Xiaole Han and Masatoshi Sakairi. The promotion effect of aluminium ion on hydrogen entry into steel during atmospheric corrosion. *Electrochimica Acta*, 458 (2023) 142505.

[3] Xiaole Han and Masatoshi Sakairi. Role of hygroscopic chloride salts on corrosion performance and hydrogen absorption of steel under cyclic wet-dry conditions. *Corrosion Science*, 231 (2024) 111993.

(Others)

[4] Adane Adugna Ayalew, Xiaole Han, Keita Suzuki, Suzuka Yoshida, and Masatoshi Sakairi. Fabrication of Ni-microstructure through electrochemical deposition using 3D printed solution flow type microdroplet cell. *Materials Today Communications*, 37 (2023) 107069.

[5] Adane Adugna Ayalew, Xiaole Han, and Masatoshi Sakairi. A critical review of additive material manufacturing through electrochemical deposition techniques. *Additive Manufacturing*, 77 (2023) 103796.

[6] Adane Adugna Ayalew, Xiaole Han, and Masatoshi Sakairi. Effect of substrate temperature and electrolyte composition on the fabrication of through-hole porous AAO membrane with SF-MDC. *Materials Chemistry and Physics*, 323 (2024) 129658.

[7] Adane Adugna Ayalew, Xiaole Han, Yoganandan Govindaraj, and Masatoshi Sakairi. Formation of Through-Hole Porous Anodic Aluminum Oxide Layer Locally with 3D Printed Solution Flow Type Microdroplet Cell. *Journal of The Electrochemical Society*, 2024 (in press).

Conference presentations:

[1] Xiaole Han and Masatoshi Sakairi, “Corrosion and hydrogen absorption of steel under salt droplets”,コロージョン・ドリーム 2023 若手研究者セミナー, 那覇, Dec. 2023.

[2] Xiaole Han and Masatoshi Sakairi, “The Role of Metal Cations in Hydrogen Absorption Into Steel Under Salt Deposits During Atmospheric Corrosion”, 74th Annual ISE Meeting, ise233261, Lyon, France, Sept. 2023.

[3] Xiaole Han and Masatoshi Sakairi, “Corrosion morphology and hydrogen absorption of steel under salt deposits during atmospheric corrosion”, Annual congress of the European Federation of Corrosion, 43457, Brussels, Belgium, Aug. 2023.

[4] Xiaole Han and Masatoshi Sakairi, “Promotion effect of Al ions on hydrogen absorption into steel under wet-dry cycle corrosion”, the Electrochemical Methods in Corrosion Research (EMCR) International conference 2022, N˚405047, France, Sept. 2022.

[5] Xiaole Han and Masatoshi Sakairi, “Effect of Chloride Salts on Hydrogen Permeation Behavior of Steel During Wet/Dry Corrosion”, 72nd Annual Meeting of the International Society of Electrochemistry, Jeju Island, Korea/Online, Aug. 2021.

[6] Xiaole Han and Masatoshi Sakairi, “Hydrogen permeation behavior of steel during wet/dry corrosion under different relative humidity and salts”, 第 68 回材料と環境討論会, Online, Oct. 2021.

[7] Xiaole Han and Masatoshi Sakairi, “Effect of Mixed Salts on Hydrogen Permeation Behavior of Steel During Wet/Dry Corrosion”, 材料と環境 2021, Online, May 2021.

[8] Xiaole Han and Masatoshi Sakairi, “Effect of metal cations on hydrogen permeation behavior of steel during wet/dry corrosion at the salt deposited area”, 化学系学協会北海道支部 2021 年冬季研究発表会, Online, Jan. 2021.

[9] Xiaole Han and Masatoshi Sakairi, “Hydrogen Permeation Behavior of Steels under Different Relative Humidity During Wet/Dry Corrosion”, 第 67 回材料と環境討論会, Online, Oct. 2020.

[10] Xiaole Han and Masatoshi Sakairi, “Effects of Relative Humidity on Hydrogen Permeation Behavior of Steels During Wet/Dry Corrosion”, 2019 年度日本鉄鋼協会・日本金属学会両北海道支部合同冬季講演大会, 札幌, Jan. 2020.

Award:

Xiaole Han, 若手講演優秀賞, “Hydrogen Permeation Behavior of Steels under Different Relative Humidity During Wet/Dry Corrosion”, 腐食防食学会, Oct. 2020.